Monthly Notices
of the
ROYAL ASTRONOMICAL SOCIETY

MNRAS **512,** 5601–5619 (2022)
Advance Access publication 2022 March 24

https://doi.org/10.1093/mnras/stac805

Stellar proper motions in the outskirts of classical dwarf spheroidal galaxies with *Gaia* EDR3

Yuewen Qi (齐玥雯) [1,2]★ Paul Zivick,[1,2] Andrew B. Pace [3] Alexander H. Riley [1,2] and Louis E. Strigari [1,2]

[1]*Mitchell Institute for Fundamental Physics and Astronomy, Texas A&M University, College Station, TX 77843, USA*
[2]*Department of Physics and Astronomy, Texas A&M University, College Station, TX 77843, USA*
[3]*McWilliams Center for Cosmology, Carnegie Mellon University, 5000 Forbes Ave, Pittsburgh, PA 15213, USA*

Accepted 2022 March 17. Received 2022 March 15; in original form 2021 November 19

ABSTRACT

We use *Gaia* EDR3 data to identify stars associated with six classical dwarf spheroidals (dSphs) (Draco, Ursa Minor, Sextans, Sculptor, Fornax, Carina) at their outermost radii, beyond their nominal King stellar limiting radius. For all of the dSphs examined, we find radial velocity matches with stars residing beyond the King limiting radius and with >50 per cent astrometric probability (four in Draco, two in Ursa Minor, eight in Sextans, two in Sculptor, 12 in Fornax, and five in Carina), indicating that these stars are associated with their respective dSphs at high probability. We compare the positions of our candidate 'extra-tidal' stars with the orbital tracks of the galaxies, and identify stars, both with and without radial velocity matches, that are consistent with lying along the orbital track of the satellites. However, given the small number of candidate stars, we cannot make any conclusive statements about the significance of these spatially correlated stars. Cross matching with publicly available catalogues of RR Lyrae, we find one RR Lyrae candidate with >50 per cent astrometric probability outside the limiting radius in each of Sculptor and Fornax, two such candidates in Draco, nine in Ursa Minor, seven in Sextans, and zero in Carina. Follow-up spectra on all of our candidates, including possible metallicity information, will help confirm association with their respective dSphs, and could represent evidence for extended stellar haloes or tidal debris around these classical dSphs.

Key words: stars: kinematics and dynamics – Galaxy: fundamental parameters – Galaxy: kinematics and dynamics.

1 INTRODUCTION

The structure and kinematics of classical dwarf spheroidal galaxies (dSphs) (Draco, Sculptor, Ursa Minor, Carina, Sextans, Fornax, Leo I, and Leo II) have long been a subject of interest (Mateo 1998; McConnachie 2012; Battaglia, Helmi & Breddels 2013a). Radial velocity (RV) dispersion measurements (Walker et al. 2007) show that dSphs are among the most dark-matter-dominated galaxies known, and they may be used as a probe of the nature of dark matter on the smallest scales (Bullock & Boylan-Kolchin 2017). Though astrometric data are not yet as sensitive to internal dispersions as RV data (Strigari, Frenk & White 2018), these data sets have potential to provide significantly more information on the dSphs dark matter haloes than RVs alone. Previous studies have largely focused on the kinematics and structure of dSphs by studying the stars within their main bodies, i.e. their stellar limiting radii.

Models of the kinematics of dSphs typically assume that these systems are in dynamical equilibrium. However, since they have been accreted into and evolved within the Milky Way (MW) potential, it is certain that they have lost some amount of mass due to tidal stripping. For subhaloes that host luminous galaxies, tidal stripping may be imprinted in the observed phase space distribution of the stars. This stripping is most prominent in the Sagittarius dwarf galaxy, which has tidal tails that extend hundreds of degrees from the main body (Newberg et al. 2002; Majewski et al. 2003; Koposov et al. 2012; Ibata et al. 2020). At much lower luminosities, $\sim 10^3$ $L_\odot$, the Tucana III ultra-faint dwarf galaxy has associated streams that are likely due to tidal disruption (Drlica-Wagner et al. 2015; Shipp et al. 2018; Mutlu-Pakdil et al. 2018; Li et al. 2018). There are possible hints of tidal disruption of other satellite galaxies, but the evidence remains inconclusive (Carlin & Sand 2018; Mutlu-Pakdil et al. 2019, 2020; Gregory et al. 2020; Longeard et al. 2021).

Though they do not yet exhibit clear evidence of tidal disruption, photometric and RV studies have been effective in identifying stars associated with Carina, Ursa Minor, and Draco at radii beyond their classical King limiting radius (Muñoz et al. 2005, 2006a). For the classical dSphs that have been modelled, there is a wide degree of mass-loss scenarios possible that still lead to a galaxy that is visible in its current state (Munoz, Majewski & Johnston 2008; Penarrubia et al. 2009; Battaglia, Sollima & Nipoti 2015; Ural et al. 2015; Wang et al. 2017). Stars may be stripped off of these galaxies, though at this time the surface brightness of the associated streams could be well below photometric limits of their detection (Wang et al. 2017; Genina et al. 2020).

In recent years, deep photometric measurements of dSphs (Muñoz et al. 2018; Wang et al. 2019) and kinematic data from the *Gaia* satellite (Gaia Collaboration 2018b) have substantially improved our understanding of the present state and evolution of the dSphs. From

★ E-mail: yuewenq@tamu.edu

the *Gaia* data, the proper motions (PMs) of the entire population of dSphs have become available, leading to an improved characterization of their full three-dimensional motions (Fritz et al. 2018; Gaia Collaboration 2018b; Simon 2018; Pace & Li 2019; McConnachie & Venn 2020b). In addition to the bulk motions, *Gaia* EDR3 data have led to, in some cases, the first identification of a small rotation, or streaming, component of the stars in the classical dSphs (Martínez-García et al. 2021). Though the bulk motions and the streaming components may be extracted, the internal velocity dispersions of $\sim$10 km s^{-1} are still unable to be resolved by *Gaia* data in itself (see however Massari et al. 2018, 2020).

Though the bulk motions of the dSphs are well characterized via the photometry and kinematics of stars within their main bodies, less well understood are their stellar associations at large radii near the stellar tidal limit of these systems. Identifying member stars at large radii is important, as it can shed light on the extent of the dark matter halo of the dSphs, or possibly determine whether the systems are undergoing tidal disruption (Deason et al. 2021). In addition, it may be the first indication of an extended stellar halo associated with dSphs, which would yield important information on their star formation histories.

With this motivation, in this paper we use *Gaia* EDR3 to study the kinematics of a population of six classical dSphs: Draco, Sculptor, Ursa Minor, Carina, Sextans, Fornax. These dSphs are chosen as a representative sample because of their relative proximities and the high-quality astrometry for their brightest stars. In addition, the deduced early infall times (Rocha, Peter & Bullock 2012; Fillingham et al. 2019) make them good candidates in which these effects may be observed. Since our method for identifying stars at large radii is motivated by the *Gaia* astrometry, it provides an independent and powerful new probe of member stars at large radii as compared to the photometric studies discussed above.

This paper is organized as follows. In Section 2, we review the *Gaia* data and our selection criteria. In Section 3, we discuss our methodology for identifying member stars in dSphs. In Section 4, we present our results for the number of stars associated with each dSph at large radius, cross matches with RV and RR Lyrae surveys, and a discussion of the position of our candidates with respect to the orbital motion of each dSph. In Section 5, we present our discussion and conclusions.

2 DATA SELECTION

Expanding upon earlier data releases from the *Gaia* mission (Gaia Collaboration 2016), *Gaia* Early Data Release 3 (EDR3, Gaia Collaboration 2021) has substantially reduced the statistical uncertainties for individual stellar PMs and reduced systematic uncertainties for the full PM catalogue. Here, we use the EDR3 data to study regions of interest around six classical dSphs, with a goal of identifying candidate member stars at the largest possible projected radii from them.

The properties of the six classical dSphs that we study are shown in Table 1. We choose these six dSphs because they are the optimal combination of the nearest and the brightest classical dSphs. As indicated, all systems have very similar ellipticities, and their half-light radii vary in a range of $\sim$0.1–1 kpc. The RVs and the velocity dispersions for these dSphs are well measured, and estimates of their mass distributions from these data sets indicate that they all are dark matter dominated (Battaglia, Helmi & Breddels 2013b). Only for Draco and Sculptor (Massari et al. 2018, 2020) are internal tangential velocity dispersions measured, though they are substantially less well constrained than the RV measurements.

Table 1. Properties of each of the dSphs in our sample.

Galaxy	α [deg]	δ [deg]	M_V	$D_\odot$ [kpc]	Θ_p [deg]	ϵ	$r_{h,p}$ [arcmin]	$r_{h,p}$ [kpc]	$r_{t,k}$ [arcmin]	$r_{t,k}$ [kpc]	V_r [km s^{-1}]	σ_v [km s^{-1}]
Draco	260.0517	57.9153	-8.71 ± 0.05	76	87	0.29	9.67 ± 0.09	0.214	48.1 ± 1.3	1.064	-291.7	9.1
Ursa Minor	227.2854	67.2225	-9.03 ± 0.05	76	50	0.55	18.3 ± 0.11	0.407	77.3 ± 0.7	1.709	-247.2	9.5
Sextans	153.2625	-1.6147	-8.72 ± 0.06	86	57	0.30	16.5 ± 0.10	0.413	60.5 ± 0.6	1.514	224.3	7.9
Sculptor	15.0392	-33.7092	-10.82 ± 0.14	86	92	0.33	11.17 ± 0.05	0.280	74.1 ± 0.4	1.854	111.4	9.2
Fornax	39.9971	-34.4492	-13.46 ± 0.14	147	45	0.29	19.6 ± 0.08	0.838	69.1 ± 0.4	2.955	55.2	11.7
Carina	100.4029	-50.9661	-9.43 ± 0.05	105	60	0.36	10.1 ± 0.10	0.308	58.4 ± 0.98	1.784	222.9	6.6

Note. The columns are: (1) galaxy name; (2) and (3): position (McConnachie & Venn 2020a); (4) magnitude; (5) distance; (6) position angle based on Plummer models; (7) ellipticity; (8) Plummer half-light radius (in arcmin); (9) Plummer half-light radius (in kpc for the reader's reference); (10) King limiting radius, with the exception of Fornax using Battaglia et al. (2006); (11) King limiting radius (in kpc for the reader's reference); (12) radial velocity; (13) radial velocity uncertainties. (4) to (11) are from Muñoz et al. (2018). (12) and (13) are from Simon (2019).

To select a candidate sample of stars associated with each dSph, we perform a series of cuts through a sequence of several steps. First, we apply a cut to select sources in EDR3 which are within a fixed projected radius from the centre of each dSph. Specifically, we select stars within a projected radius of 3° around each dSph. This radius corresponds to around 10 times the projected half-light radius for all of the dSphs, which provides sufficient sample size to characterize the populations of the main body and the MW foreground.

Once these cuts have been implemented, to produce an astrometrically well-behaved sample we consider only stars with reliable astrometric solutions. Specifically, we keep only sources that pass the following EDR3 cut criteria:

(i) $|C^*| \leq 3\sigma_{C^*}(G)$
(ii) `ruwe` < 1.4
(iii) `ipd_gof_harmonic_amplitude` ≤ 0.2
(iv) `visibility_periods_used` ≥ 9
(v) `astrometric_excess_noise_sig` ≤ 2
(vi) `ipd_frac_multi_peak` ≤ 2
(vii) `astrometric_params_solved` > 3
(viii) no `duplicated_source` in EDR3.

Here, $|C^*|$ is the corrected BP and RP flux excess factor (as defined in equation 6 of Riello et al. 2021), $\sigma_{C^*}(G)$ is defined in equation (18) of Riello et al. (2021), and `ruwe` is the renormalized unit weight error provided in EDR3 catalogue. We then remove any known active galactic nucleus in *Gaia* EDR3 (Gaia Collaboration 2021) to reduce contamination. We correct the G-band magnitude and the flux excess factor as suggested in Riello et al. (2021), and the *Gaia* dust extinctions for G and G_{RP} assuming relations from Gaia Collaboration (2018a).

In addition to the cuts above, we perform additional cuts that are more specific to the nature of our analysis. First, we remove stars that are obvious members of the foreground by removing stars with well-measured non-zero parallaxes. This is implemented with a parallax cut as $\omega - 3\sigma_\omega < 0$, where ω is the parallax and σ_w is the error on the parallax. On top of this parallax cut, we perform a second cut by removing stars that would have a transverse velocity larger than the escape velocity of the MW at the distance of each dSph. We used the `MWPotential2014` potential in `galpy` (Bovy 2015) to determine the escape velocity ($V_{\rm esc}$) at a dSph's given distance. Specifically, we only keep stars with $4.74D_\odot(PM - 3\sigma_{PM}) \leq V_{\rm esc}$, where PM is the proper motion in the plane of the sky, and σ_{PM} is the error on the PM.

After the parallax cut, our final step to minimize MW contamination in our sample is to select stars based on their position in colour–magnitude space. To create this cut, we start by compiling publicly available spectroscopic data for each dSph (Walker, Mateo & Olszewski 2009; Battaglia et al. 2011; Hendricks et al. 2014; Walker, Olszewski & Mateo 2015; Fabrizio et al. 2016; Spencer et al. 2018; Pace et al. 2020, 2021) and cross-match these catalogues with EDR3. Then, for each dSph spectroscopic catalogue, we keep stars whose RVs are consistent within 3σ of the systemic RV (V_r) of the dSph (where σ is the velocity dispersion of the system, as listed in Table 1 along with V_r). We plot this trimmed sample in *Gaia* colour–magnitude space using G and $G - G_{RP}$ (as noted in Gaia Collaboration (2021), the G_{BP} filter suffers from bias at faint magnitudes so we choose to use only G and G_{RP} given many of our targets are near the *Gaia* faint limit). Finally, we use the position of the spectroscopically selected stars to define an area in the colour–magnitude diagram (CMD) that is consistent with the dSph (as seen in Fig. 1 for all six satellites).

After implementing all of these cuts, our final samples of stars from *Gaia* for each dSph are as follows: Draco (10 799), Ursa Minor (6215), Sextans (6219), Sculptor (8340), Fornax (21 072), and Carina (23 498).

3 LIKELIHOOD ANALYSIS

We now discuss our methodology for assigning membership probabilities to stars in each of our dSphs using both astrometric and photometric data. We note that *Gaia* RVs are not available for the stars in our sample, as they are all fainter than the magnitude limit of the DR2 RV sample. The magnitude limit of *Gaia* RVs is $G \sim 14$ which is brighter than the tip of the red-giant branch in every galaxy, and *Gaia* DR2 RVs are brighter than this. As we discuss next, while we achieve accurate membership results using PMs alone, we include information on the spatial distribution through photometry along with the PM data to improve upon the model and further eliminate the influence of MW foreground stars. The methods discussed here follow those established in Pace & Li (2019); we review the salient aspects for our analysis.

For stars in our catalogue, we adopt the orthographic projection of RA and Dec. and PMs from Gaia Collaboration (2018b), and transform them into the Cartesian frame as

$$\begin{aligned} x &= \cos\delta \sin(\alpha - \alpha_C) \\ y &= \sin\delta \cos\delta_C - \cos\delta \sin\delta_C \cos(\alpha - \alpha_C), \end{aligned} \tag{1}$$

where α and δ are the location of a star in the RA and Dec. direction, and (α_C, δ_C) is the centre of the dSph. After completing the transformation, we begin our analysis by assuming our catalogue is composed of two populations: a general MW foreground/background population and members of the dSph. As in Pace & Li (2019), we define the total likelihood function as

$$\mathcal{L} = f_{sat}\mathcal{L}_{sat} + (1 - f_{sat})\mathcal{L}_{MW}. \tag{2}$$

The likelihood is composed of two components. First, the component $\mathcal{L}_{sat}$ describing the stars that belong to the dSph, and second, the component $\mathcal{L}_{MW}$ describing the MW foreground/background stars. The quantity $f_{\rm sat}$ is defined as the fraction of stars that belong to the dSph, so that $1 - f_{\rm sat}$ represents the fraction of stars that belong to the MW foreground/background.

The likelihood components $\mathcal{L}_{sat}$ and $\mathcal{L}_{MW}$ can be broken up into two components, one that depends on the kinematics through the PMs, and one that depends on the spatial distribution. Adding in these components, the likelihood takes the form

$$\begin{aligned} \mathcal{L} = {} & f_{sat}\mathcal{L}_{sat,spatial}\mathcal{L}_{sat,PM} \\ & + (1 - f_{sat})\mathcal{L}_{MW,spatial}\mathcal{L}_{MW,PM}, \end{aligned} \tag{3}$$

where $\mathcal{L}_{sat,spatial}$ and $\mathcal{L}_{sat,PM}$ correspond to the photometric and PM likelihoods for the dSph, and $\mathcal{L}_{MW,spatial}$ and $\mathcal{L}_{MW,PM}$ are the respective likelihood functions for the MW component.

For each of the dSph and MW PM components, we assume both follow independent multivariate Gaussian distributions (Vasiliev 2019):

$$\begin{aligned} \mathcal{L}_{\imath,PM} = {} & (2\pi)^{-N/2}(\det\Sigma)^{-1/2} \\ & \times \exp\left[-\frac{1}{2}\left(\mu_\imath - \mu_\imath^{mod}\right)^T \Sigma^{-1}\left(\mu_\imath - \mu_\imath^{mod}\right)\right], \end{aligned} \tag{4}$$

where N is the total number of the stars in the sample, which are given for each dSph in Section 2, and $\imath = (\rm sat, MW)$ refers to either the dSph or the MW foreground/background component. Here, $\mu_\imath$ represents the EDR3 measured PM vectors of stars that belong to a

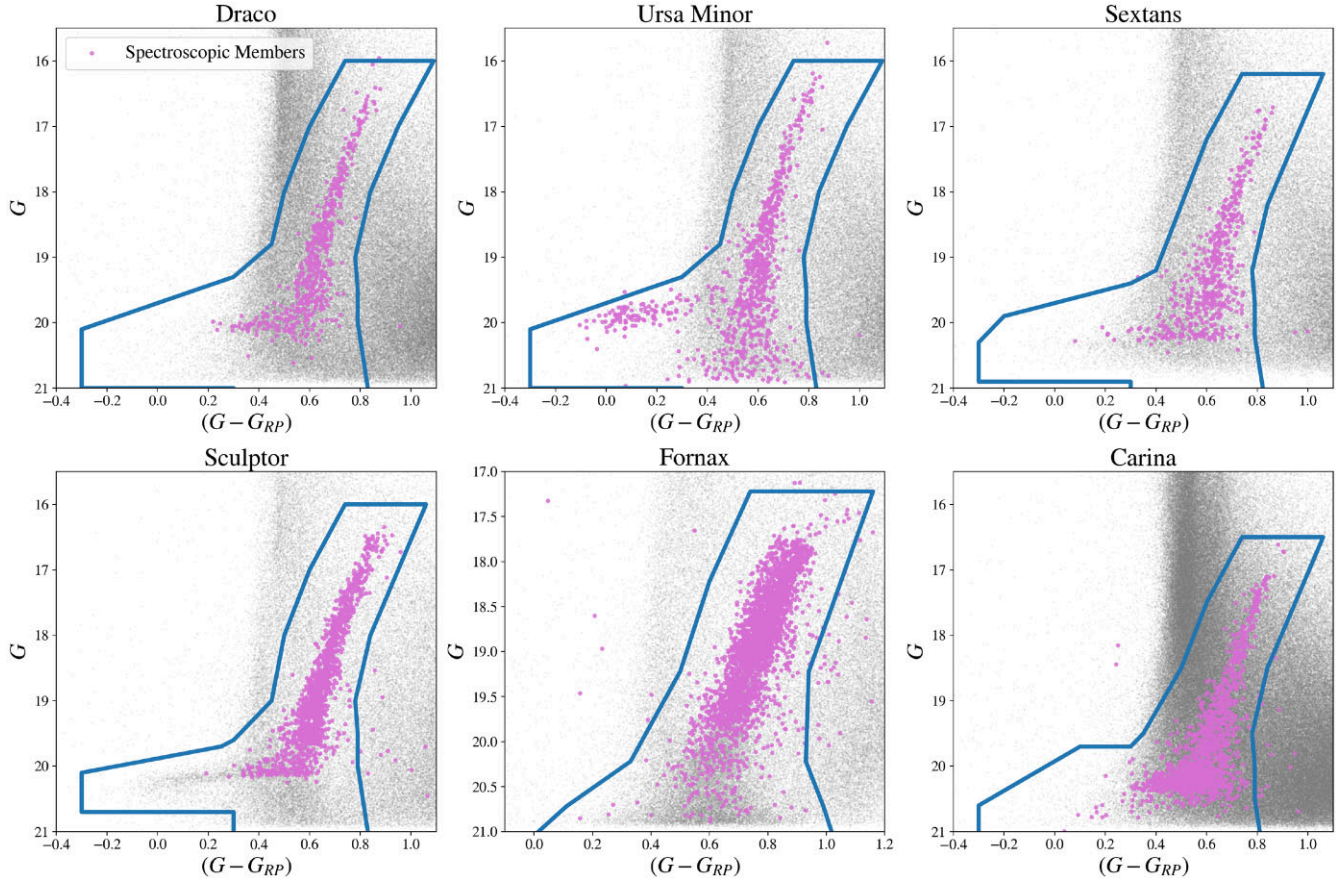

Figure 1. CMDs of the six satellite galaxies examined in this study. The grey points indicate all *Gaia* EDR3 stars within 3 deg of each satellite. The purple points indicate stars from publicly available RV catalogues that have been cross-matched with EDR3 and are consistent with the satellite for its systemic RV. Finally, the boundary used for trimming our EDR3 sample to remove contaminating MW stars is marked by the dark blue line.

given component, and μ_t^{mod} gives the expected value of the PM, and the covariance matrix Σ is defined as

$$\Sigma = \begin{bmatrix} E_1 + S_1 & 0_{2\times2} & \dots & 0_{2\times2} \\ 0_{2\times2} & E_2 + S_2 & \dots & \\ \vdots & \vdots & \ddots & \vdots \\ 0_{2\times2} & 0_{2\times2} & \dots & E_N + S_N \end{bmatrix} \tag{5}$$

with

$$E_i = \begin{bmatrix} \epsilon_{i,x}^2 & \rho_i \epsilon_{i,x} \epsilon_{i,y} \\ \rho_i \epsilon_{i,x} \epsilon_{i,y} & \epsilon_{i,y}^2 \end{bmatrix}, \quad S_i = \begin{bmatrix} \sigma_i^2(x_i) & 0 \\ 0 & \sigma_i^2(x_i) \end{bmatrix}, \tag{6}$$

where ρ_i is the EDR3-defined correlation between $\mu_{\alpha\star} = \mu_\alpha \cos\delta$ and μ_δ for each star, $\epsilon_{i,x}$ and $\epsilon_{i,y}$ are uncertainties on $\mu_{\alpha\star}$, μ_δ correspondingly, and σ_i is the modelled velocity dispersion at the location of each star.

We note that the assumption of a multivariate Gaussian is likely an oversimplification for both populations, in particular for the MW population. As we discuss next, we test the general properties of this model by comparing to the photometric data using only the kinematic components of the likelihood, and from this analysis we find good agreement with existing photometric data. For this reason we have confidence that this approach is reasonable given the current sensitivity of *Gaia*.

For the photometric model, we assume that the projected density of each dSph is described by a Plummer profile (Plummer 1911)

$$\Sigma(R_e) = \frac{1}{\pi a_h^2 (1-\epsilon)} \left(1 + R_e^2/a_h^2\right)^{-2}, \tag{7}$$

where a_h is the semimajor half-light radius, ϵ is the projected ellipticity, and R_e is the elliptical radius defined as

$$R_e^2 = R_x^2 + \frac{R_y^2}{(1-\epsilon)^2}. \tag{8}$$

Here, we rotate R_x and R_y by the position angle Θ, which is measured North to East in the frame of the sky:

$$\begin{aligned} R_x &= x\cos(\Theta) - y\sin(\Theta) \\ R_y &= x\sin(\Theta) + y\cos(\Theta), \end{aligned} \tag{9}$$

where x and y are defined in equation (1).

From the Plummer model, the normalized version of the spatial component of the likelihood function is given by

$$\mathcal{L}_{sat,spatial} = \frac{\sqrt{\left(a_h^2 + R_{\max}^2\right)\left((1-\epsilon)^2 a_h^2 + R_{\max}^2\right)}}{1-\epsilon} \times \frac{a_h^2}{R_{\max}^2 \left(a_h^2 + R_e^2\right)^2}. \tag{10}$$

With the assumption of a constant spatial distribution for the MW population, $\mathcal{L}_{MW,\mathrm{spatial}} = \frac{1}{R^2_{\mathrm{max}}}$, the spatial likelihood acts as a weighting factor preferentially selecting stars that are closer to the centre of the dSph. Note that in our analysis we have $R_{\mathrm{max}} = 3^\circ$.

We use the likelihood defined above to estimate model parameters. To estimate the best value for the parameters, we use the `emcee` library (Foreman-Mackey et al. 2013), which implements the affine-invariant ensemble sampler for Markov Chain Monte Carlo (MCMC; Goodman & Weare 2010) in Python. We free up to 10 parameters and their corresponding priors in the analysis, which are:

(i) One uniform prior between 0 and 1 for the fraction of the stars belonging to each dSph: f_{sat}

(ii) Three parameters describing the spatial distribution: one log prior for $\log_{10}(\frac{R_e}{1\ \mathrm{deg}})$ between -2 and 0; one uniform prior between 0 and 1 for ellipticity; one uniform prior between -90 and 90 deg for position angle

(iii) Two uniform priors between -1 and 1 mas yr^{-1} for parameters describing the dSph PM: $(\mu_{\alpha,\star} \equiv \mu_\alpha cos\delta,\ \mu_\delta)$

(iv) Two uniform priors between -5 and 5 mas yr^{-1} for parameters describing the MW systematic PM: $(\mu^{MW}_{\alpha,\star} \equiv \mu^{MW}_\alpha cos\delta,\ \mu^{MW}_\delta)$

(v) Two log uniform between -2 and 1 mas yr^{-1} for parameters describing the MW proper motion dispersion: ($\sigma^{MW}_{\mu_\alpha cos\delta}$ and $\sigma^{MW}_{\mu_\delta}$)

We fix the parameters that represent the intrinsic PM velocity dispersions of the dSphs to the values that are determined from their measured RV dispersions in Table 1. Note that this assumes that the velocity dispersions of all the dSphs are isotropic, but given that *Gaia* data in itself are not sensitive to the internal PM velocity dispersions, this assumption does not impact our analysis. For the position angle, the prior range is set based on the conventions in our Cartesian projection; however for final reporting, we present our best-fitting position angle in the standard literature convention of defining the position angle from North over East.

From the posterior of the `emcee` runs, we calculate the probability, $P_{i,\mathrm{PM+Spatial}}$, that the ith star belongs to the dSph as

$$P_{i,\mathrm{PM+Spatial}} = \frac{f_{sat;i}\,\mathcal{L}_{sat,spatial;i}\,\mathcal{L}_{sat,PM;i}}{\mathcal{L}_i}, \tag{11}$$

where $\mathcal{L}_i$ is the ith value in equation (3). This provides us a probability distribution of $P_{i,\mathrm{PM+Spatial}}$ of each star, which we then use to calculate the membership possibility by finding median of its $P_{i,\mathrm{PM+Spatial}}$ distribution. Following the same method, we can compute the PM-only probability, $P_{i,PM}$, for individual star i as

$$P_{i,PM} = \frac{f_{sat;i}\,\mathcal{L}_{sat,PM;i}}{f_{sat;i}\,\mathcal{L}_{sat,PM;i} + (1 - f_{sat;i})\mathcal{L}_{MW,PM;i}}. \tag{12}$$

4 RESULTS

We now move on to presenting our results for the membership probabilities for each dSph. We begin by focusing on the results obtained from the likelihood method described above. We then move on to cross-match our highest probability stars with RV measurements from each dSph and from RR Lyrae catalogues. For stars that we identify as highly probable members at large radii, we then compare to the orbital trajectories of each dSph to determine how the stars at large radii compare to the best-fitting orbits.

Before considering membership probabilities, to calibrate to previous results we first measure the systemic PM for each dSph. Specifically, we compare to the work of Gaia Collaboration (2018b) and McConnachie & Venn (2020b) for DR2, and the updated EDR3 systemic PMs from McConnachie & Venn (2020a), Battaglia et al. (2022), and Martínez-García et al. (2021). All of these works use a selection radius of $\lesssim$2 deg around each dSph, so calibrating to these results provides a test for the 3° cut radius implemented in our analysis.

In Fig. 2, we show the comparison of PMs. The error bars on our analysis represent the 1σ containment regions for the posterior of the PM. Note that there is a shift from DR2 to EDR3 in the measured PMs for each dSph, which is mostly due to the reduced systematics between the different data sets. We specifically see that our results are consistent with McConnachie & Venn (2020a), who also use EDR3 data. The value of the PMs that we obtain are listed in Table 2.

4.1 Member identification

We then move on to examine the membership probabilities. To calculate these, we consider two implementations of our likelihood analysis: one including the photometric and kinematic components ($P_{\mathrm{PM+Spatial}}$, as defined in equation 11), and one kinematics-only component (P_{PM}, as defined in equation 12). The latter implementation is in particular useful to obtain a surface brightness profile for the dSphs that is independent of previous measurements, and as described above this serves as a good test of our multivariate Guassian model.

In Fig. 3, we plot the surface brightness profiles for dSphs. We sum over P_{PM} for every star within the given radius bin divided by the area to plot the number density in red, along with the Plummer profiles in black using measurements from Muñoz et al. (2018) (see Table 1). The P_{PM} generated surface brightness profiles agree with those obtained in Muñoz et al. (2018), which gives us confidence that our multivariate Gaussian likelihood model is a good description of the systems.

Beyond the central region of the dSphs, given recent work suggesting the presence of extended stellar features around ultra-faint MW satellites (Chiti et al. 2020), we are interested in attempting to identify similar extended features around the classical dSph satellites. To this end, we can use our likelihood analysis to identify stars at large radii that are potential members of each dSph. To visualize the membership probabilities and mark potential outlying members, we set up a series of four plots for each dSph (Figs 4–9 for Draco, Ursa Minor, Sextans, Sculptor, Fornax, and Carina respectively, hereafter referred to as the membership figures). The top right and bottom left plots show the spatial distributions of all stars with $P \geq 50$ per cent, where the top right shows P_{PM} and the bottom left shows $P_{\mathrm{PM+Spatial}}$, in order to demonstrate the strong constraints placed on the membership probabilities by requiring a fit to a Plummer profile. We additionally plot multiples (2, 4, 6, and 8) of the Plummer half-light radius (along with ellipticity and position angle) from Muñoz et al. (2018) to provide a quantitative sense of the spatial extent of the dSph. The bottom right plot shows our full catalogue of stars for each dSph field of view, colour coded by P_{PM} in PM space. The top left plot shows the CMD selection used for each dSph, the density of likely MW foreground/background stars in the field of view (stars with $P_{PM} < 1$ per cent), and stars at large radii that are candidate member stars.

To discuss stars at large radii, we select a boundary to differentiate stars considered to be part of the main body and stars that comprise any extended stellar feature. For this boundary, given its common usage in discussing the tidal limit of resolved stellar populations, we choose to use the King limiting radius, $r_{t,k}$, position angle, and ellipticity from dedicated photometric work (see Table 1 for specific values). In the top right and bottom left plots in the membership

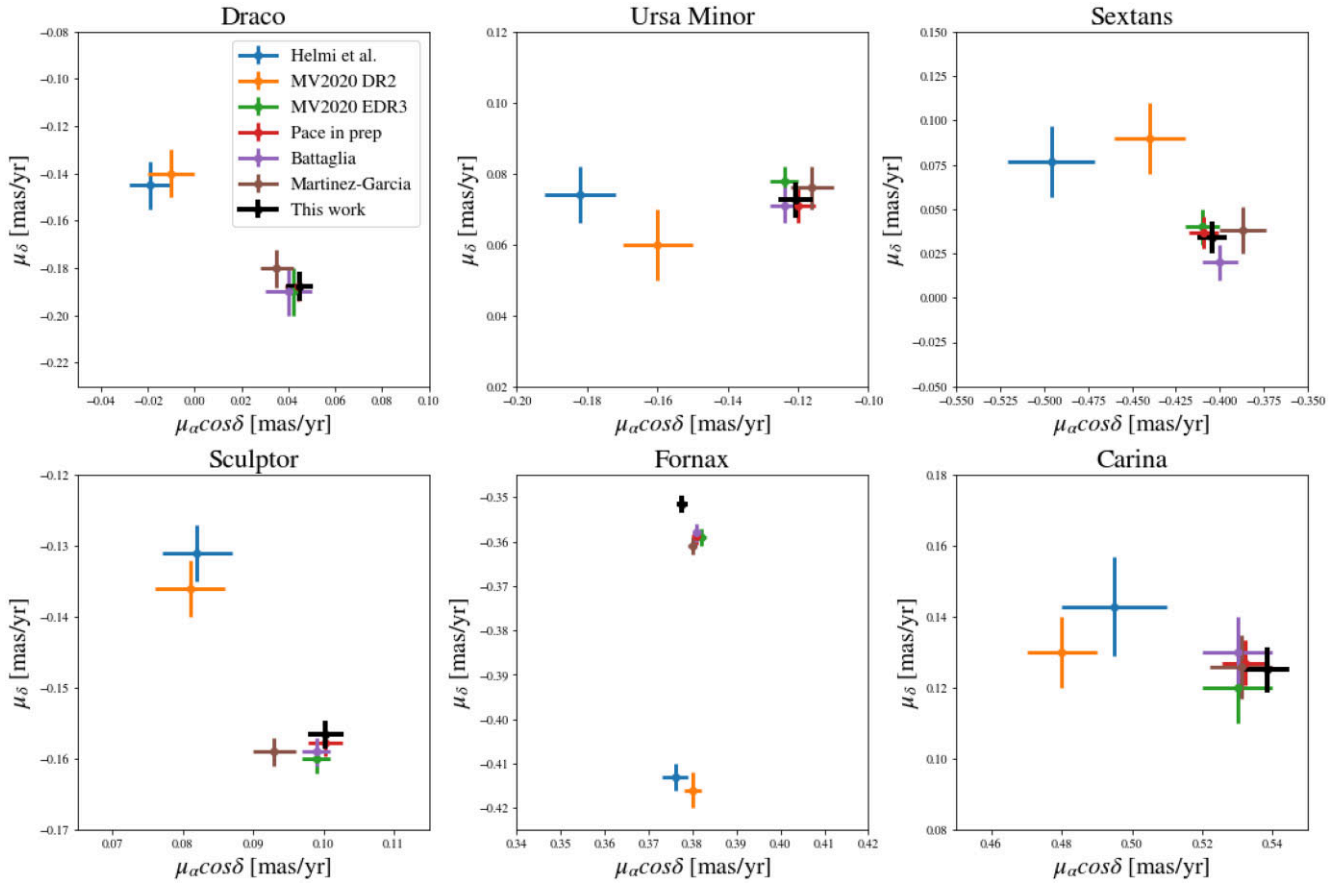

Figure 2. Comparison of systemic PMs of Draco, Ursa Minor, Sextans, Sculptor, Sextans, and Carina in $\mu_\alpha \cos\delta$ and μ_δ directions. The black error bars shows PM with 1σ uncertainties using *Gaia* EDR3. The blue error bars show Gaia Collaboration (2018b)'s value and uncertainty of PMs using *Gaia* DR2. The orange error bars show the PMs of McConnachie & Venn (2020b) using *Gaia* DR2 data, while the green error bars are the updated PMs of McConnachie & Venn (2020a) using *Gaia* EDR3. For other values based on *Gaia* EDR3, we have error bars in red representing the PMs of Pace et al. in prep. The purple crosses show PMs from Battaglia et al. (2022), and the brown crosses represent PMs of Martínez-García et al. (2021). We can see that our PM distributions are in good agreement with PM values using *Gaia* EDR3 data.

Table 2. Properties of each of the dSphs generated by MCMC. The columns are: (1) galaxy name; (2) and (3): proper motion; (4) half-light radius; (5) ellipticity; (6) position angle (measured North to East).

Galaxy	$\mu_\alpha cos\delta$ [mas yr^{-1}]	μ_δ [mas yr^{-1}]	a_H [arcmin]	ϵ	pa [deg]
Draco	0.045 ± 0.006	−0.188 ± 0.006	8.97 ± 0.25	0.29 ± 0.02	90.73 ± 2.73
Ursa Minor	−0.121 ± 0.005	0.073 ± 0.005	18.83 ± 0.48	0.49 ± 0.02	51.16 ± 1.18
Sextans	−0.404 ± 0.009	0.034 ± 0.009	22.87 ± 0.77	0.25 ± 0.03	53.35 ± 3.57
Sculptor	0.100 ± 0.003	−0.157 ± 0.002	12.05 ± 0.16	0.30 ± 0.01	94.66 ± 1.16
Fornax	0.378 ± 0.001	−0.352 ± 0.002	18.50 ± 0.14	0.33 ± 0.01	39.75 ± 0.59
Carina	0.538 ± 0.006	0.125 ± 0.006	10.64 ± 0.28	0.37 ± 0.02	63.17 ± 1.94

figures, we display this boundary as a red ellipse and mark in red any stars that sit beyond this boundary and have $P_{PM} \geq 90$ per cent, labelling them as extra-tidal candidates (which are then also displayed in the upper left CMD plot and the bottom right PM plot in the membership figures).

The locations of the extra-tidal candidates in CMD space may be compared against the MW foreground/background contours as a way to assess potential MW contamination. For several systems (Draco, Ursa Minor, Sextans, and Carina) we see a clear separation between our high-probability members and the MW population. This provides us with strong hints that these stars are indeed associated with the dSphs, even though we have not directly included any information about colours or magnitudes in the likelihood analysis. The properties of all extra-tidal candidates (with dust-corrected $G < 19.0$) are shown in Tables A1–A4 (a table with all extra-tidal candidates down to our limiting magnitude of $G \sim 20.8$ is available in machine-readable format).

As a first initial check on what kind of contamination we might expect, we test our methodology on a simulated dwarf galaxy orbiting an MW-like host. In particular, we use the Aurigaia catalogues (Grand et al. 2018) which are mock observations, based on *Gaia* DR2 systematics, of select Auriga simulations (Grand et al. 2017). After

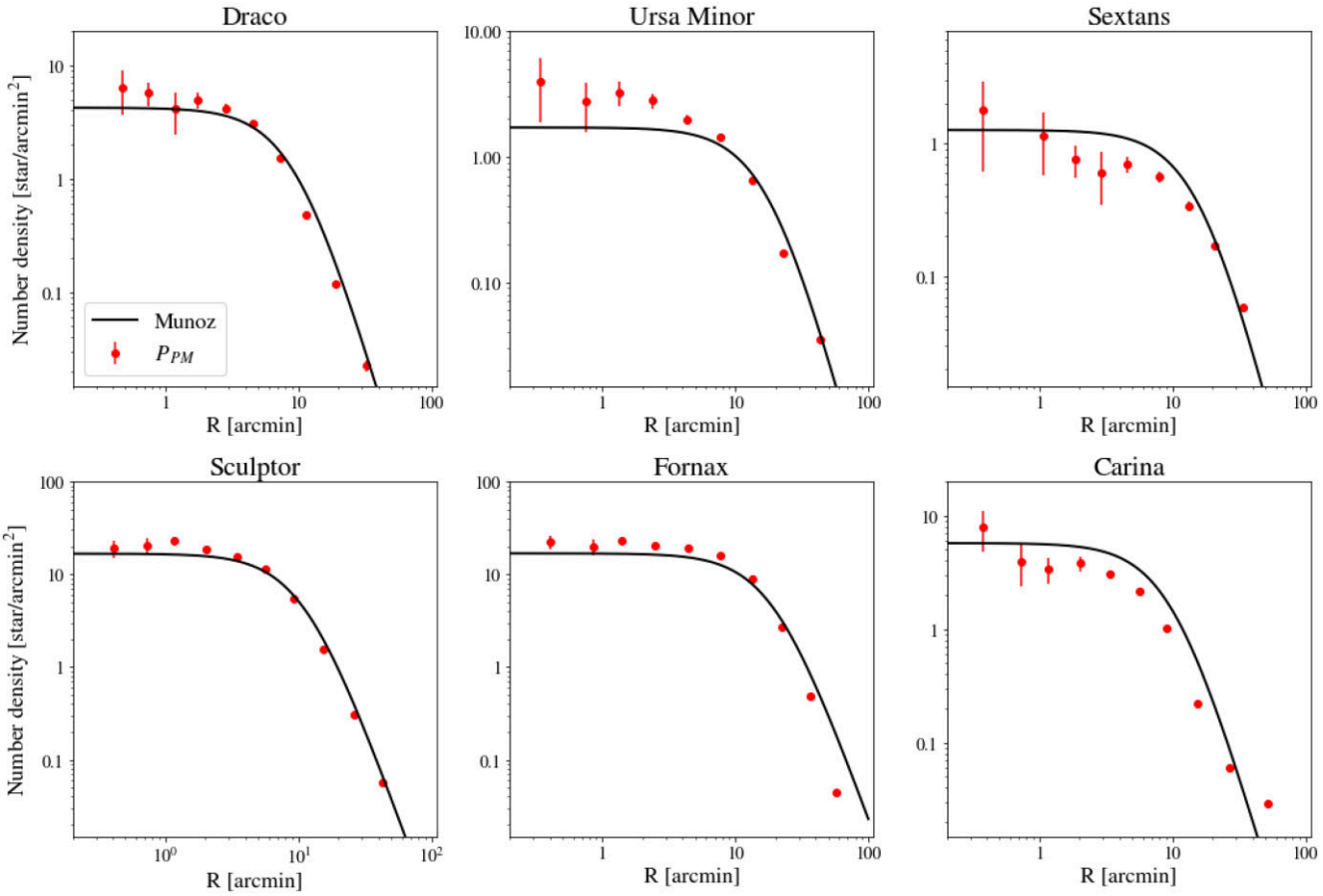

Figure 3. The surface brightness based on MCMC generated PM-only membership probability (P_{PM}) in red, comparing with the Plummer model in black from Muñoz et al. (2018). The number densities in red are calculated using the sum of P_{PM} for every star in the given bin divided by the area, while the error bars represent the square root of the sum of P_{PM} for every star in the given bin divided by the area.

applying the same cuts and processing the data with our MCMC framework, we find that 0.16 per cent of the nearby 'MW' stars pass the $P_{PM} \geq 90$ per cent cut and 2.35 per cent pass the $P_{PM} \geq 50$ per cent cut. To translate that to our specific dSphs examined we can use the full EDR3 sample as an expected upper limit. In the case of Draco with 3226 stars, we would expect 5.05 stars pass the $P_{PM} \geq 90$ per cent cut and 75.73 stars pass the $P_{PM} \geq 50$ per cent cut. When we compare that with our identified extra-tidal candidate stars for Draco (18 stars with $P_{PM} \geq 90$ per cent and 167 stars with $P_{PM} \geq 50$ per cent), we see this suggests our extra-tidal candidates to likely be a real feature.

4.2 Cross match with RR Lyrae

Given this plausible extra-tidal signal, we want to independently assess the membership of these stars as a check on our PM-only probabilities (P_{PM}). One way of determining whether a star belongs to a given satellite would be using distance estimates, like the ones provided for variable stars. In particular, RR Lyrae serve as an excellent map of substructure in the halo, so we can search for RR Lyrae near the centre of each satellite that have magnitudes within 0.3 dex in G (corresponding to a distance tolerance of $\sim$10 kpc for our closer satellites) from the Horizontal Branch (HB) of that satellite.

For this, we compile a collection of variable star catalogues and cross-match each one with all stars in the *Gaia* EDR3 catalogue (with no cuts applied) for each satellite field of view. We combine each cross-matched catalogue together, using the *Gaia* EDR3 `source_id` column to create a unique list of RR Lyrae. We then use the *Gaia* magnitudes to select all RR Lyrae within 0.3 dex of the HB for the satellite. Finally, we compare the final positions of these HB-consistent RR Lyrae against the King limiting radius, $r_{t,k}$, for each satellite. As discussed in Section 2, we make a series of cuts to select astrometically well-behaved stars, some of which preferentially remove variable stars. As such, for this RR Lyrae check, we hold off on cross-matching the RR Lyrae with our astrometric catalogue until the final step to check against our probabilities. Next, we list the number of RR Lyrae we find in *Gaia* EDR3 for each satellite, the full list of catalogues we find matching RR Lyrae in, the number that are consistent in distance with the satellite, the number of those outside $r_{t,k}$, and of the extra-tidal RR Lyrae, the number that have a match in our $P_{PM} \geq 50$ per cent catalogue.

4.2.1 Draco

We find 357 unique RR Lyrae (Kinemuchi et al. 2008; Drake et al. 2013a,b; Palaversa et al. 2013; Drake et al. 2014; Samus' et al. 2017; Sesar et al. 2017; Clementini et al. 2019) in our full EDR3 catalogue. From those 357 RR Lyrae, 286 have a magnitude consistent with the distance of Draco with 10 sitting outside $r_{t,k}$. 2 of these 10 are present in our astrometrically cleaned catalogue and have $P_{PM} \geq 50$ per cent (as marked in Fig. 4).

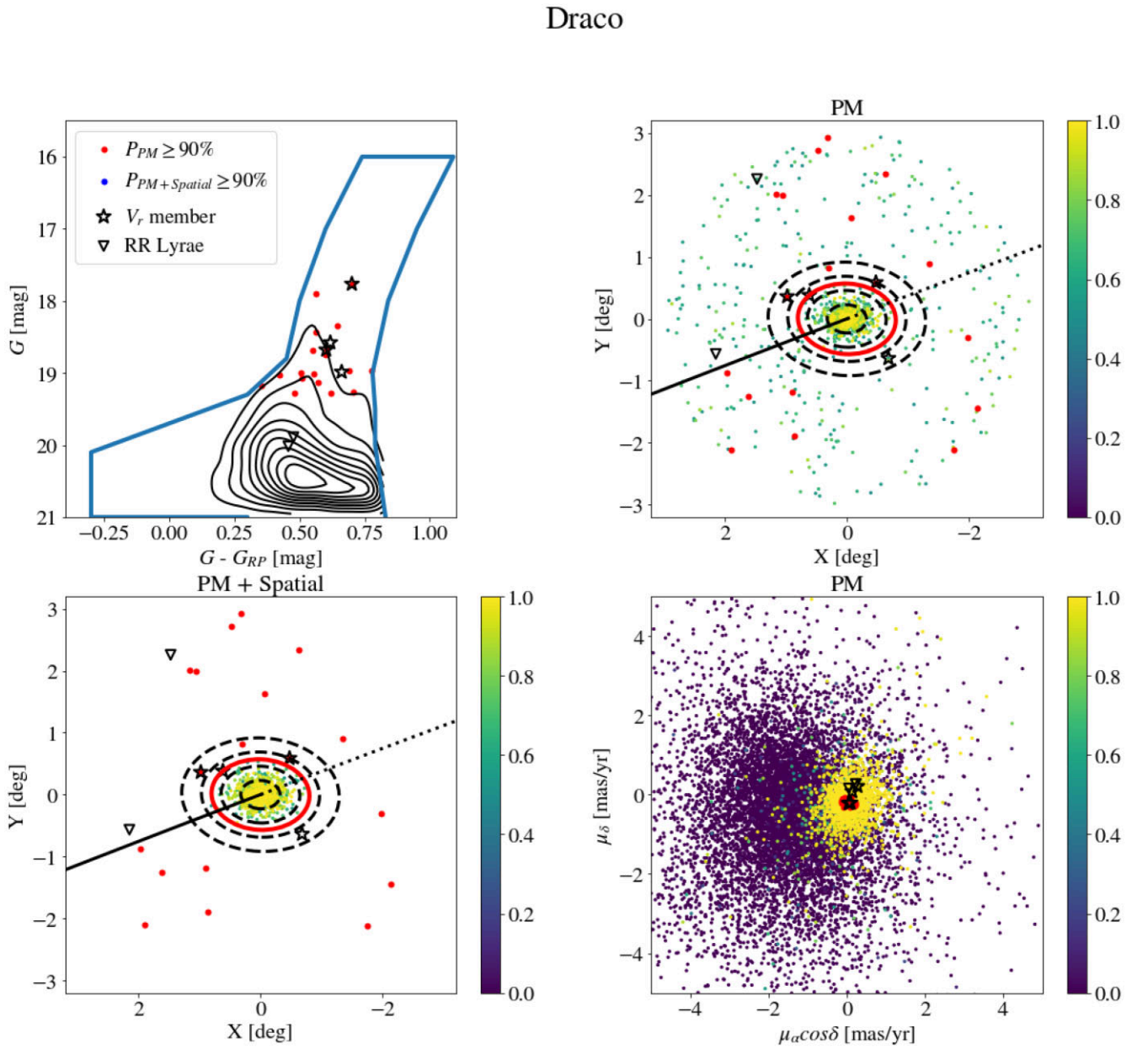

Figure 4. In the upper left panel we have the identified possible extra-tidal candidates ($P_{PM} \geq 90$ per cent) using PM-only membership probability (in red) and PM plus spatial membership probability ($P_{\rm PM+Spatial} \geq 90$ per cent in blue) with our CMD selection for Draco. The black contour lines show the density of likely MW foreground/background stars in the CMD selection (stars with $P_{PM} < 1$ per cent). The star symbols represent the V_r members, which are stars with cross-matched RV that are consistent with the bulk velocity of Draco (RV within $3\sigma_v$ of V_r in Table 1). The upside down triangles show the cross-matched RR Lyrae that are consistent in distance with Draco. Both G and G_{RP} have been corrected (see Section 2). Upper right panel: Stars with their PM-only membership probability of $P_{\rm PM} \geq 50$ per cent distribution for Draco in X-Y coordinates centred at 0, colour-coded with P_{PM} from 0 to 1, labelled with extra-tidal candidates. The red ellipse represents the $r_{t,k}$ transformed by position angle and ellipticity. The black dashed ellipses show $2r_{h,p}$, $4r_{h,p}$, $6r_{h,p}$, $8r_{h,p}$ transformed by position angle and ellipticity, respectively. We can see that the candidates and higher probability stars are concentrated in the middle. We also show the orbit of the satellite forwards (backwards) in time as a solid (dotted) black line. Lower left panel: Stars with their PM + Spatial membership probability of $P_{\rm PM+Spatial} \geq 50$ per cent, colour-coded with $P_{\rm PM+Spatial}$ from 0 to 1, are being shown in X-Y coordinates. Lower right panel: PMs distribution for our full *Gaia* EDR3 catalogue for Draco, centred at 0, colour-coded with P_{PM} from 0 to 1. We can see that the candidates and higher probability stars are concentrated in the middle.

4.2.2 *Ursa minor*

We find 175 unique RR Lyrae (Palaversa et al. 2013; Drake et al. 2014; Sesar et al. 2017; Clementini et al. 2019) in our full EDR3 catalogue. From those 175 RR Lyrae, 128 have a magnitude consistent with the distance of Ursa Minor with 12 sitting outside $r_{t,k}$. Nine of these 12 are present in our catalogue and have $P_{PM} \geq 50$ per cent (as marked in Fig. 5).

4.2.3 *Sextans*

We find 249 unique RR Lyrae (Vivas et al. 2004, 2019; Drake et al. 2013a,b, 2014; Palaversa et al. 2013; Samus' et al. 2017; Sesar et al. 2017; Clementini et al. 2019) in our full EDR3 catalogue. We do note the presence of the globular cluster Palomar 3 in our field of view and mask out the area around the cluster, which removes nine RR Lyrae for a total of 274 RR Lyrae remaining. Of those 274, 222 have

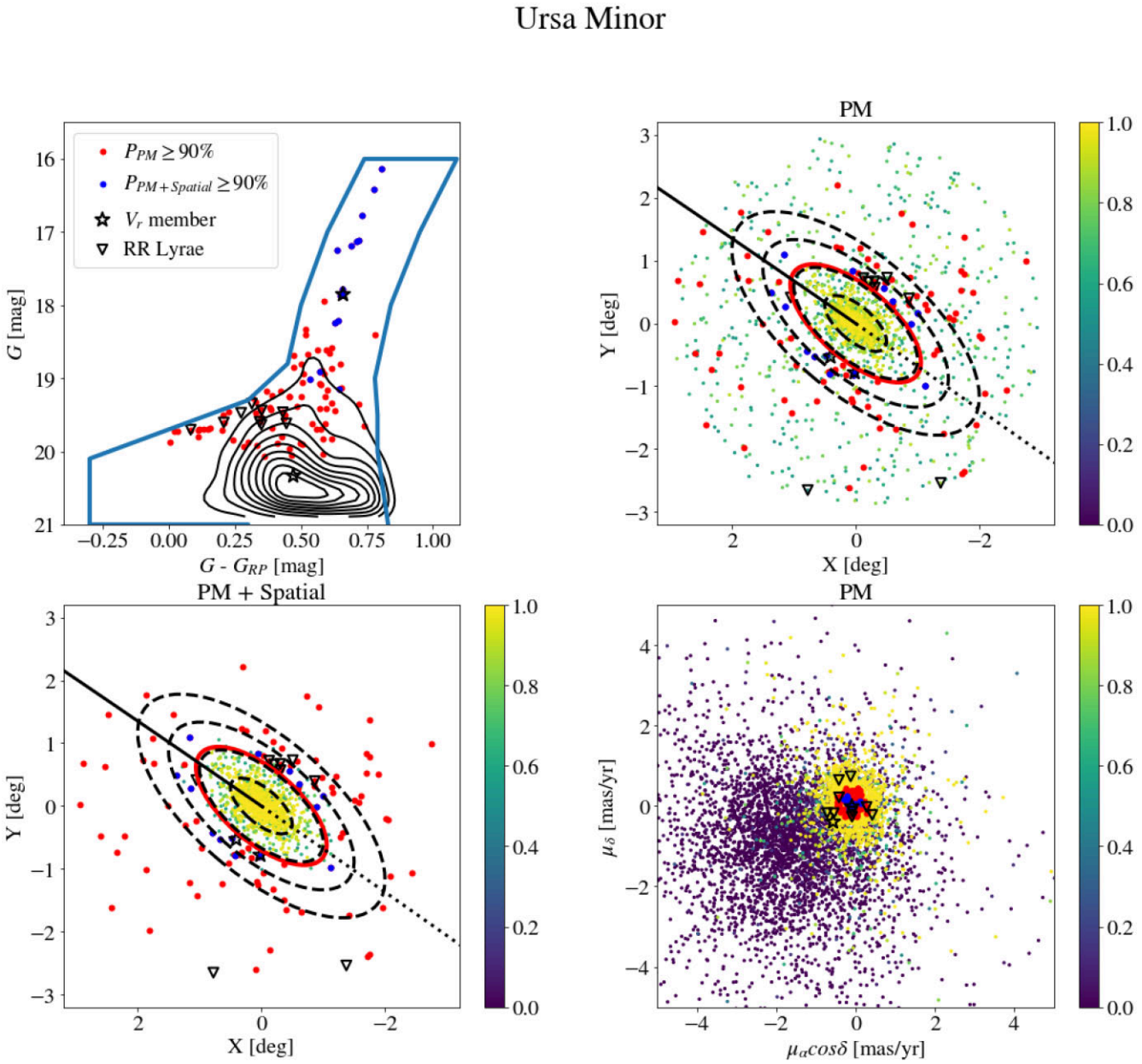

Figure 5. Same format as Fig. 4 for Ursa Minor.

a magnitude consistent with the distance of Sextans with 21 sitting outside $r_{t,k}$. Seven of those 21 are present in our catalogue and have $P_{PM} \geq 50$ per cent (as marked in Fig. 6).

4.2.4 *Sculptor*

We find 482 unique RR Lyrae (Torrealba et al. 2015; Drake et al. 2017; Clementini et al. 2019; Stringer et al. 2021) in our full EDR3 catalogue. From those 482 RR Lyrae, 456 have a magnitude consistent with the distance of Sculptor with two sitting outside $r_{t,k}$. One of these two are present in our catalogue and have $P_{PM} \geq 50$ per cent (as marked in Fig. 7).

4.2.5 *Fornax*

We find 67 unique RR Lyrae (Torrealba et al. 2015; Drake et al. 2017; Clementini et al. 2019; Stringer et al. 2021) in our full EDR3 catalogue. From those 67, 31 have a magnitude consistent with the distance of Fornax with four sitting outside $r_{t,k}$. One of these four is present in our catalogue and has $P_{PM} \geq 50$ per cent (as marked in Fig. 8).

4.2.6 *Carina*

We find 82 unique RR Lyrae (Vivas & Mateo 2013; Torrealba et al. 2015; Drake et al. 2017; Clementini et al. 2019) in our full EDR3 catalogue. From those 82 RR Lyrae, 44 have magnitudes consistent with the distance of Carina with one sitting outside $r_{t,k}$ but that star does not have $P_{PM} \geq 50$ per cent, so there are no such joint candidates for Carina.

As a general note, we do not claim original detections of extratidal RR Lyrae for most of the satellites above. Nearly all of the satellites in this paper have had dedicated work in examining their RR Lyrae populations. And indeed, many of them note the presence of RR

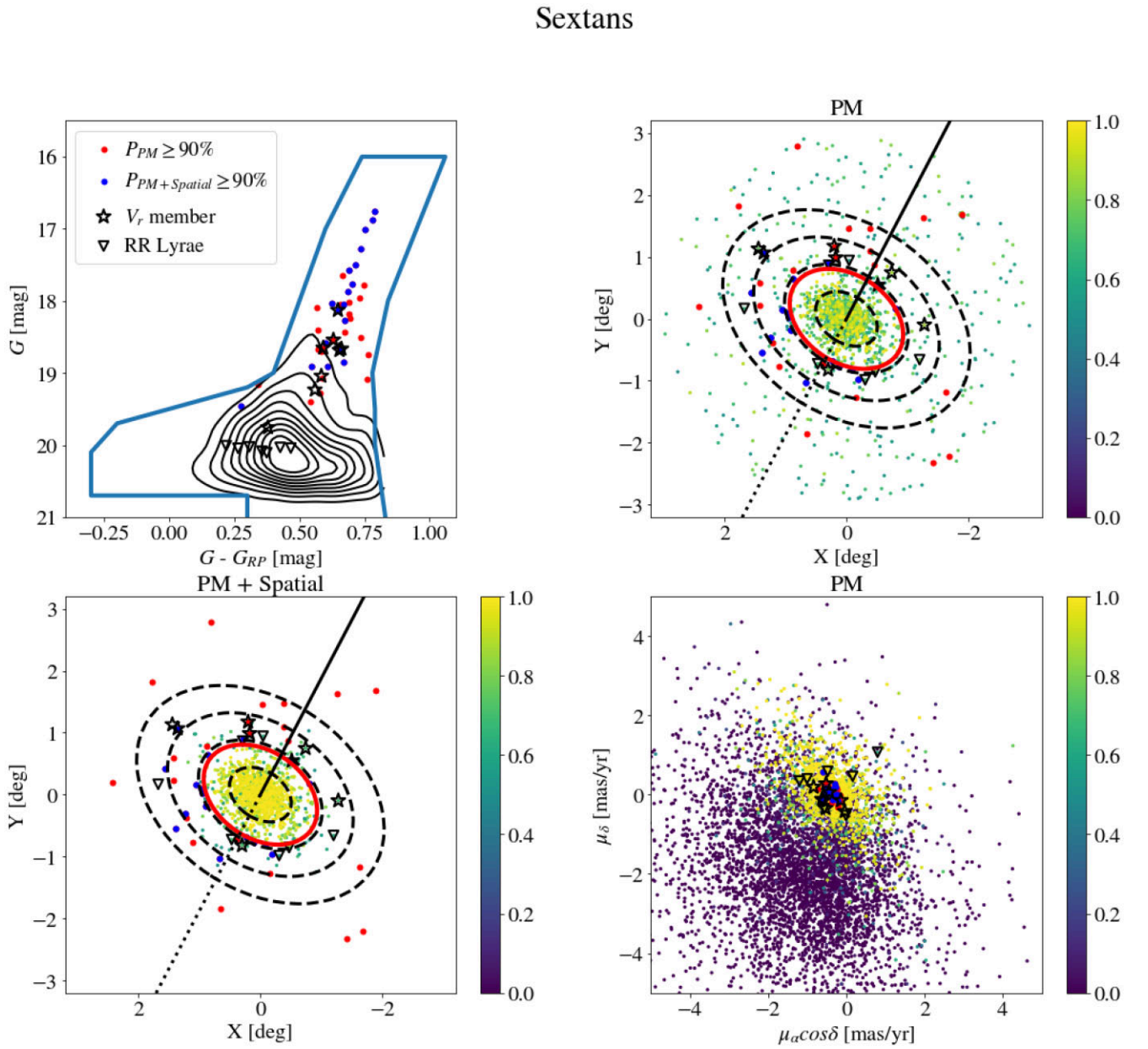

Figure 6. Same format as Fig. 4 for Sextans.

Lyrae consistent with the satellite that lay outside the tidal radius. For two of these satellites, Fornax and Carina, we do not attempt a rigorous comparison to the literature (Vivas & Mateo 2013 for Carina and Stringer et al. 2021 for Fornax) as their distance places a significant fraction of the RR Lyrae in the satellite at a magnitude fainter than our *Gaia* magnitude limit. However, even with our limited sample, we find qualitative agreement between our work and the literature in the distribution of RR Lyrae, with Carina being mostly tightly clustered within the tidal radius and Fornax spilling over the tidal radius.

With respect to the other satellites, we find good agreement with published results for Draco (Muraveva et al. 2020), including the extension in the south-west direction in the RR Lyrae population. Intriguingly, they did not examine too far beyond the King limiting radius for Draco, so our two most outlying PM-consistent RR Lyrae candidate members are absent from their analysis. For both Sextans (Medina et al. 2018; Vivas et al. 2019) and Sculptor (Martínez-Vázquez et al. 2016) we also recover the extended structure present in them. Ursa Minor is the only one of the six without a publicly available dedicated analysis, so we were unable to compare our results. Taken as a whole, the identification of a majority of RR Lyrae in our PM membership sample, despite the astrometric quality cuts, the consistency with published results, and still finding matches to RR Lyrae in the extratidal candidates, is encouraging evidence for the robustness of our methodology.

4.3 Cross match with RVs

For our sample of high-probability stars, we search the literature for stars that have existing RVs. If a given star does indeed have RV consistent with the bulk RV of the dSph, it would give us both high

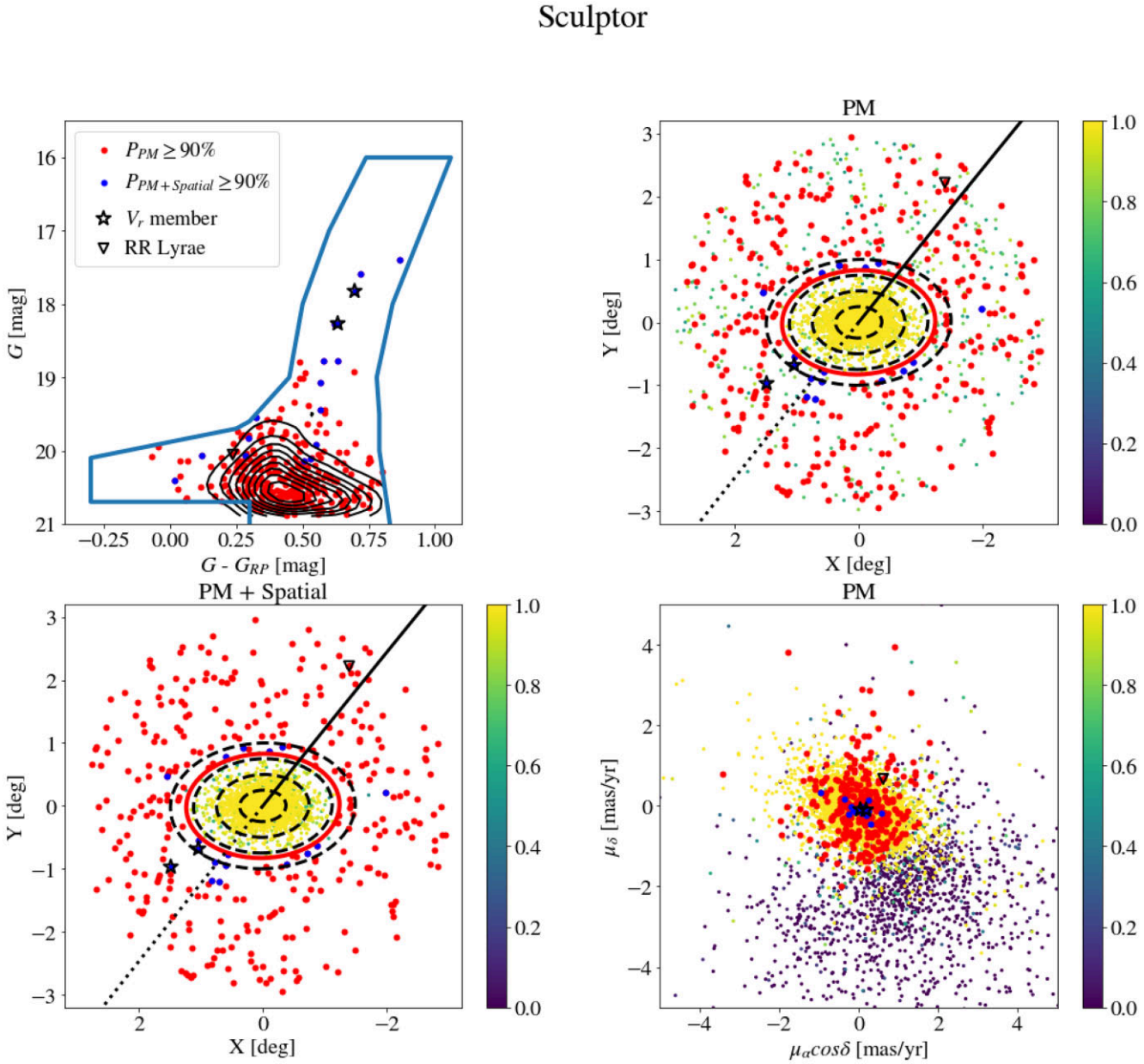

Figure 7. Same format as Fig. 4 for Sculptor.

confidence in our analysis method, as well as a confirmation that the star is an associated member of the dSph.

We compile a collection of RV catalogues and cross-match each one with our *Gaia* EDR3 catalogue (see Section 2). We then keep only stars with consistent RV (within $3\sigma_v$ of V_r, Table 1) in our RV catalogues. In our consistent RV catalogues, we define a star with $P_{PM} \geq 50$ per cent as a V_r member. Next, we list the number of RV matches we find in our full *Gaia* EDR3 catalogue for each satellite, the full list of catalogues we find matching RV in, the number that are consistent in the bulk RV, and of the RV beyond King limiting radius, the number that have $P_{PM} \geq 50$ per cent, and bright (dust-corrected $G \leq 19$) stars with $P_{PM} \geq 90$ per cent.

4.3.1 *Draco*

We find 636 stars with RV data (Walker et al. 2015; Spencer et al. 2018) in our full EDR3 catalogue. From those 505 have RV that are within $3\sigma_v$ of the RV as obtained from Simon (2019), hereafter S19 (see Table 1). From those 505 stars, 425 have $P_{PM} \geq 50$ per cent, with four sitting outside $r_{t,k}$ (see V_r member in Fig. 4), suggesting more candidates may be identified with considering stars with lower membership probabilities. Out of the 10 brightest ($G \leq 19$) possible candidates ($P_{PM} \geq 90$ per cent) beyond the King limiting radius in Table A1, we find two stars with matching RVs. These two stars are labelled with red stars in Fig. 4.

4.3.2 *Ursa Minor*

We find 762 stars with RV data (Spencer et al. 2018; Pace et al. 2020) in our full EDR3 catalogue. From those 731 have RV that are within $3\sigma_v$ of the RV as obtained from S19. From those 731 stars, 665 have $P_{PM} \geq 50$ per cent, with two sitting outside $r_{t,k}$ (Fig. 5). Out of the 30 brightest ($G \leq 19$) possible candidates in Table A1, we find one star with matching RVs.

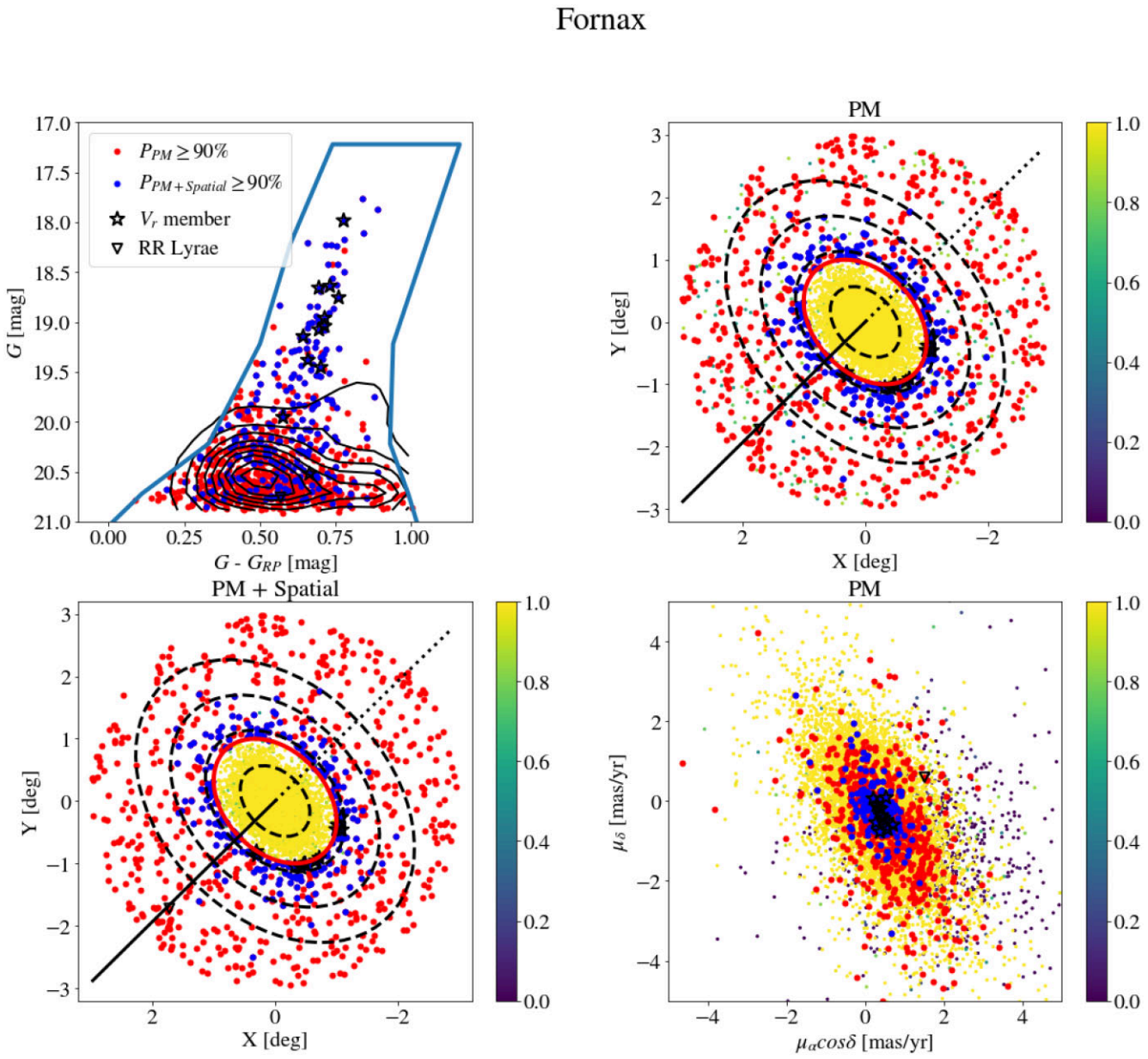

Figure 8. Same format as Fig. 4 for Fornax.

4.3.3 *Sextans*

We find 540 stars with RV data (Battaglia et al. 2011; Walker et al. 2009, 2015) in our full EDR3 catalogue. From those 478 have RV that are within $3\sigma_v$ of the RV as obtained from S19. Among them, 412 have ≥50 per cent PM-only membership probability, with eight sitting outside $r_{t,k}$ (Fig. 6). Out of the 34 brightest possible candidates in Table A2, we find four stars with matching RVs.

4.3.4 *Sculptor*

We find 1423 stars with RV data (Walker et al. 2009, 2015) in our full EDR3 catalogue. From those 1370 have RV that are within $3\sigma_v$ of the RV as obtained from S19. Among them, 1355 have ≥50 per cent PM-only membership probability, with two sitting outside $r_{t,k}$ (Fig. 7). Out of the 10 brightest possible candidates in Table A2, we find two stars with matching RVs.

4.3.5 *Fornax*

We find 2721 stars with RV data (Walker et al. 2009; Hendricks et al. 2014; Pace et al. 2021) in our full EDR3 catalogue. From those 2667 have RV that are within $3\sigma_v$ of the RV as obtained from S19. Among them, 2662 have ≥50 per cent PM-only membership probability, with 12 sitting outside $r_{t,k}$ (Fig. 8). Out of the 30 brightest possible candidates in Table A3, we find five stars with matching RVs.

4.3.6 *Carina*

We find 1443 stars with RV data (Muñoz et al. 2006b; Walker et al. 2009; Fabrizio et al. 2016) in our full EDR3 catalogue. From those 1190 have RV that are within $3\sigma_v$ of the RV as obtained from S19. Among them, 717 have ≥50 per cent PM-only membership probability, with five sitting outside $r_{t,k}$ (Fig. 9). Out of the 39

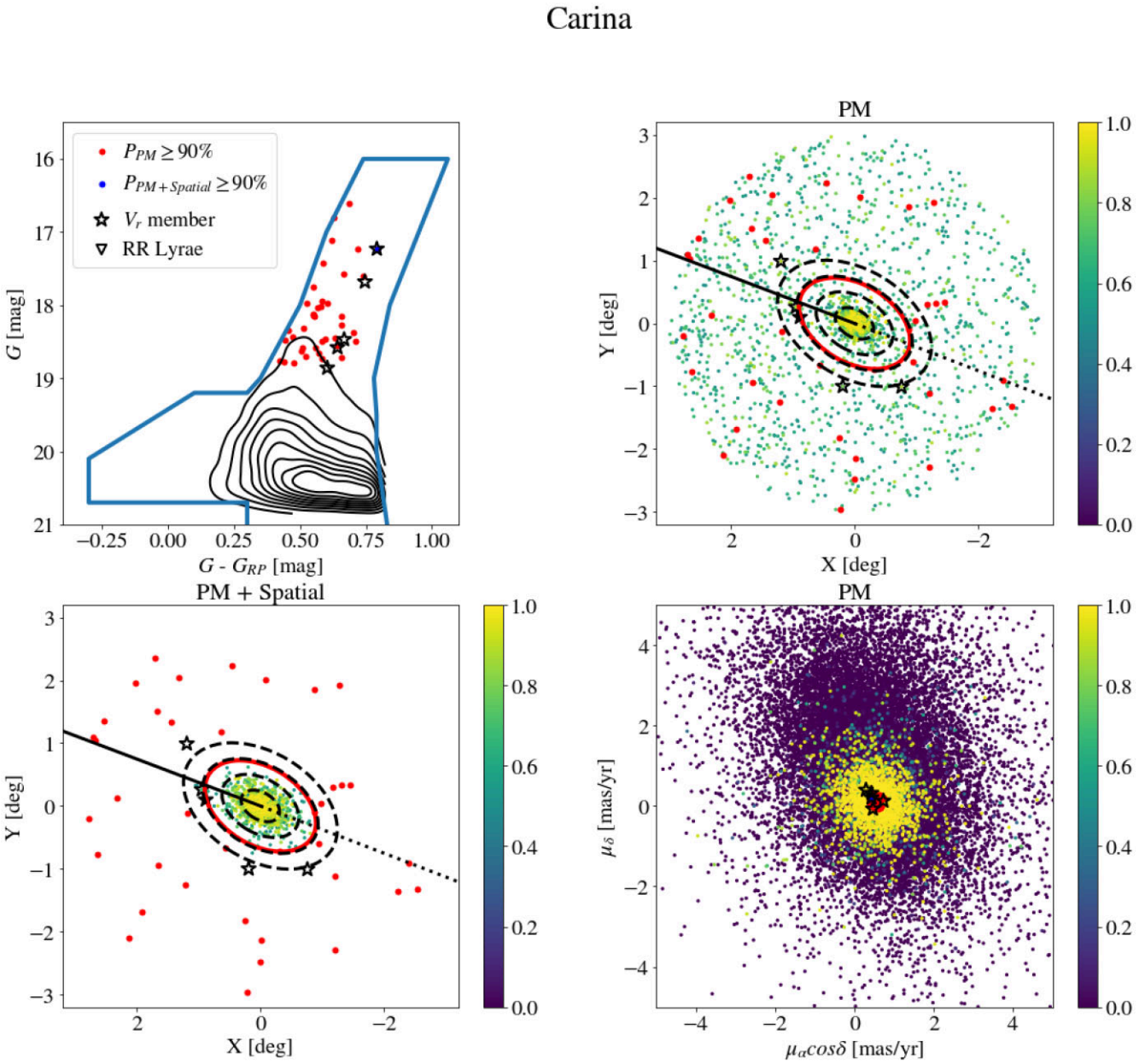

Figure 9. Same format as Fig. 4 for Carina.

brightest possible candidates in Table A4, we find one star with matching RVs.

4.4 Orbits

Tidal debris from disrupting satellites generally aligns spatially with the orbit of the progenitor (Dehnen et al. 2004; Montuori et al. 2007), a fact that can be used to associate stellar streams with previously known objects (Ibata et al. 2019; Hansen et al. 2020; Bonaca et al. 2021). We compute orbits for each satellite using `gala` (Price-Whelan 2017) to see if our high-probability candidates are found near the orbital track. We represent the potential of the MW using a four-component model composed of a spherical Hernquist bulge (Hernquist 1990), a spherical Hernquist nucleus, an axisymmetric Miyamoto–Nagai disc (Miyamoto & Nagai 1975), and a spherical Navarro–Frenk–White dark matter halo (Navarro, Frenk & White 1996), with parameters fixed to their default values in `gala` (v1.3; Price-Whelan et al. 2020). We assume the on-sky coordinates, distance, and RV for each satellite as compiled in Table 1 and the PMs derived in this work from Table 2. To convert these heliocentric observations to a Galactocentric frame, we adopt a distance from the Sun to the Galactic centre of $R_0 = 8.122$ kpc (Gravity Collaboration 2018), a height of the Sun relative to the Galactic plane of $z_0 = 20.8$ pc (Bennett & Bovy 2019), and a solar motion relative to the Galactic centre of (12.9, 245.6, 7.78) km s^{-1} (Reid & Brunthaler 2004; Drimmel & Poggio 2018; Gravity Collaboration 2018).

In general, our extratidal PM-only candidates ($P_{PM} \geq$ 90 per cent) are distributed roughly uniform along the sky, with some candidates lying very close to the orbital track. PM+spatial candidates ($P_{\rm PM+Spatial} \geq 90$ per cent) tend to lie within 1 deg of the orbit track, but this is largely expected due to the spatial component of the likelihood penalizing large on-sky separations from the satellite,

which lies (naturally) along the orbit. We particularly highlight Sculptor, where two of the four PM+spatial candidates and the confirmed RV member lie very close to the trailing orbit, as well as Draco, whose one RV member is within 1 deg of the leading orbit. Extratidal candidates that lie close to the satellite's orbital track but far from the satellite itself are promising targets for spectroscopic follow-up.

5 DISCUSSION AND CONCLUSION

We have used *Gaia* EDR3 astrometry data to identify stars associated with six classical dSphs (Draco, Ursa Minor, Sextans, Sculptor, Fornax, Carina) at their outermost radii. Using a Gaussian mixture model to describe the PM distributions for the member stars and for the background of each dSph, we identify a substantial population of candidate associations for each dSph. All of our astrometric members are consistent with the CMDs for each dSph. In summary, we identify a list of extra-tidal candidates ($P_{PM} \geq 90$ per cent) in all six dSphs. We find 18 extra-tidal candidates in Draco, 95 extra-tidal candidates in Ursa Minor, 40 extra-tidal candidates in Sextans, 334 extra-tidal candidates in Sculptor, 844 extra-tidal candidates in Fornax, and 39 extra-tidal candidates in Carina. We use simulation to calculate that 0.16 per cent of the MW stars pass the $P_{PM} \geq 90$ per cent cut, and suggest that our extra-tidal candidates to likely be a real feature.

Since our methodology for assigning membership probabilities does not include any information on RV or distance, when cross-matching with RV samples and RR Lyrae catalogues in the literature, we use $P_{PM} \geq 50$ per cent stars to include more matches.

Using this cross-match, we identify a list of candidates outside the King limiting radius in all six dSphs consistent with both RV and astrometry data. From this RV matching, we find four candidates in Draco, two in Ursa Minor, eight in Sextans, two in Sculptor, 12 in Fornax, and five in Carina, indicating that these stars are associated with their respective dSphs at high probability. This provides strong kinematic evidence for the existence of member stars associated with the dSphs outside of their classical stellar King limiting radius.

In order to further improve membership assessment, we have additionally cross-matched our samples of candidates to RR Lyrae catalogues. Restricting to stars with astrometric membership probability of $P_{PM} \geq 50$ per cent, we find one RR Lyrae candidate outside the limiting radius in both Sculptor and Fornax. We find two such candidate for Draco, nine for Ursa Minor, and seven for Sextans. No matches with our $P_{PM} \geq 50$ per cent catalogue were found outside the limiting radius for Carina.

At this stage, we are not able to determine whether the aforementioned candidates represent an extended stellar halo component, or possibly even tidal debris that has been removed from the main body of the dSph due to interactions with the MW gravitational potential. If the candidate stars that we identify above are associated with tidal debris from the dSphs, it may be the case that these candidate stars line up along the orbital track of the dSph. Using updated estimates for the orbital tracks for each dSph, and models for the potential of the MW dark matter halo, we compare the projected spatial distribution of the star candidates to the best-fitting orbital tracks for each dSph. In the case of Sculptor, we find possible alignment between the orbital tracks and our stellar candidates, while for the remaining dSphs the stellar candidates are more or less randomly distributed relative to the orbital tracks. Further precision measurements of the orbits of dSphs and firm identification of member stars at large radii will improve the prospects for identifying faint tidal debris around dSphs.

The candidate stars that we have identified, both those candidates that are associated with RR Lyrae and those that are not, provide an optimal sample of candidate stars for spectroscopic follow-up. RVs and metallicities can be used to confirm the membership of our distant candidates. In particular for the RR Lyrae member candidates, both astrometry and RVs would complete a full 6D phase-space coverage on the kinematic properties of these stars.

Though current *Gaia* data are not sensitive to the measurement of internal tangential velocity dispersions of dSphs ($\sim$10 km s^{-1}), it is possible that future *Gaia* data releases will come close to, or measure, these dispersions. For this reason for the analysis in this paper, we have fixed the internal velocity dispersions of the dSphs. However, the formalism that we have implemented in this paper may be naturally extended to measure or places bounds on the tangential dispersions of dSphs with forthcoming data. In addition, the most distant stars are ideal for constraining potential rotation or velocity gradients.

Though in this paper we have assumed Gaussian models for the velocity distributions of the foreground and background, the modelling in this paper may ultimately be improved upon by constructing alternative models for the velocity distributions, in particular for that of the foreground. The formalism we have presented may be adapted to numerical simulations of the distribution which generate a population of dSphs in an MW-like halo, which includes stellar halo components. Examining such simulated haloes would both provide a sense of how the foregrounds may differ from the Gaussian model that we have assumed, and also a sense of the biases that are incurred using a Gaussian model as we have implemented.

ACKNOWLEDGEMENTS

LES acknowledges support from DOE Grant de-sc0010813. This work was supported by a Development Fellowship from the Texas A&M University System National Laboratories Office. ABP is supported by NSF grant AST-1813881. AHR acknowledges support from an NSF Graduate Research Fellowship through Grant DGE-1746932. We are grateful to Rob Grand for providing us data on the properties of dwarf galaxies in the Auriga simulation.This work used Python Programming Language, and software packages including `JUPYTER` (Kluyver et al. 2016), `ASTROPY` (Astropy Collaboration 2013, 2018), `GALPY` (Bovy 2015), `NUMPY` (Harris et al. 2020), `SCIPY` (Virtanen et al. 2020), and `CORNER.PY` (Foreman-Mackey 2016). This research has used NASA's Astrophysics Data System for bibliographic services.

This work presents results from the European Space Agency (ESA) space mission *Gaia*. *Gaia* data are being processed by the Gaia Data Processing and Analysis Consortium (DPAC). Funding for the DPAC is provided by national institutions, in particular the institutions participating in the *Gaia* MultiLateral Agreement (MLA). The *Gaia* mission website is https://www.cosmos.esa.int/gaia. The *Gaia* archive website is https://archives.esac.esa.int/gaia.

DATA AVAILABILITY

The data underlying this article will be shared on reasonable request to the corresponding author.

REFERENCES

Astropy Collaboration, 2013, A&A, 558, A33
Astropy Collaboration, 2018, AJ, 156, 123
Battaglia G. et al., 2006, A&A, 459, 423
Battaglia G., Tolstoy E., Helmi A., Irwin M., Parisi P., Hill V., Jablonka P., 2011, MNRAS, 411, 1013

Battaglia G., Helmi A., Breddels M., 2013a, New Astron. Rev., 57, 52
Battaglia G., Helmi A., Breddels M., 2013b, New Astron. Rev., 57, 52
Battaglia G., Sollima A., Nipoti C., 2015, MNRAS, 454, 2401
Battaglia G., Taibi S., Thomas G. F., Fritz T. K., 2022, A&A, 657, A54
Bennett M., Bovy J., 2019, MNRAS, 482, 1417
Bonaca A. et al., 2021, ApJ, 909, L26
Bovy J., 2015, ApJS, 216, 29
Bullock J. S., Boylan-Kolchin M., 2017, ARA&A, 55, 343
Carlin J. L., Sand D. J., 2018, ApJ, 865, 7
Chiti A., Frebel A., Jerjen H., Kim D., Norris J. E., 2020, ApJ, 891, 8
Clementini G. et al., 2019, A&A, 622, A60
Deason A. J., Bose S., Fattahi A., Amorisco N. C., Hellwing W., Frenk C. S., 2021, MNRAS, 511, 4044
Dehnen W., Odenkirchen M., Grebel E. K., Rix H.-W., 2004, AJ, 127, 2753
Drake A. J. et al., 2013a, ApJ, 763, 32
Drake A. J. et al., 2013b, ApJ, 765, 154
Drake A. J. et al., 2014, ApJS, 213, 9
Drake A. J. et al., 2017, MNRAS, 469, 3688
Drimmel R., Poggio E., 2018, Res. Notes Am. Astron. Soc., 2, 210
Drlica-Wagner A. et al., 2015, ApJ, 813, 109
Fabrizio M. et al., 2016, ApJ, 830, 126
Fillingham S. P. et al., 2019, preprint (arXiv:1906.04180)
Foreman-Mackey D., 2016, J. Open Source Softw., 1, 24
Foreman-Mackey D., Hogg D. W., Lang D., Goodman J., 2013, PASP, 125, 306
Fritz T. K., Battaglia G., Pawlowski M. S., Kallivayalil N., van der Marel R., Sohn S. T., Brook C., Besla G., 2018, A&A, 619, A103
Gaia Collaboration, 2016, A&A, 595, A1
Gaia Collaboration, 2018a, A&A, 616, A10
Gaia Collaboration, 2018b, A&A, 616, A12
Gaia Collaboration, 2021, A&A, 649, A1
Genina A., Read J. I., Fattahi A., Frenk C. S., 2020, MNRAS, 510, 2186
Goodman J., Weare J., 2010, Commun. Appl. Math. Comput. Sci., 5, 65
Grand R. J. J. et al., 2017, MNRAS, 467, 179
Grand R. J. J. et al., 2018, MNRAS, 481, 1726
Gravity Collaboration, 2018, A&A, 615, L15
Gregory A. L. et al., 2020, MNRAS, 496, 1092
Hansen T. T., Riley A. H., Strigari L. E., Marshall J. L., Ferguson P. S., Zepeda J., Sneden C., 2020, ApJ, 901, 23
Harris C. R. et al., 2020, Nature, 585, 357
Hendricks B., Koch A., Walker M., Johnson C. I., Peñarrubia J., Gilmore G., 2014, A&A, 572, A82
Hernquist L., 1990, ApJ, 356, 359
Ibata R. A., Bellazzini M., Malhan K., Martin N., Bianchini P., 2019, Nat. Astron., 3, 667
Ibata R., Bellazzini M., Thomas G., Malhan K., Martin N., Famaey B., Siebert A., 2020, ApJ, 891, L19
Kinemuchi K., Harris H. C., Smith H. A., Silbermann N. A., Snyder L. A., La Cluyzé A. P., Clark C. L., 2008, AJ, 136, 1921
Kluyver T. et al., 2016, in Loizides F., Schmidt B., eds, Positioning and Power in Academic Publishing: Players, Agents and Agendas. IOS Press, p. 87
Koposov S. E. et al., 2012, ApJ, 750, 80
Li T. S. et al., 2018, ApJ, 866, 22
Longeard N. et al., 2021, preprint (arXiv:2107.10849)
Majewski S. R., Skrutskie M. F., Weinberg M. D., Ostheimer J. C., 2003, ApJ, 599, 1082
Martínez-García A. M., del Pino A., Aparicio A., van der Marel R. P., Watkins L. L., 2021, MNRAS, 505, 5884
Martínez-Vázquez C. E. et al., 2016, MNRAS, 462, 4349
Massari D., Breddels M. A., Helmi A., Posti L., Brown A. G. A., Tolstoy E., 2018, Nat. Astron., 2, 156
Massari D., Helmi A., Mucciarelli A., Sales L. V., Spina L., Tolstoy E., 2020, A&A, 633, A36
Mateo M. L., 1998, ARA&A, 36, 435
McConnachie A. W., 2012, AJ, 144, 4
McConnachie A. W., Venn K. A., 2020a, Res. Notes Am. Astron. Soc., 4, 229
McConnachie A. W., Venn K. A., 2020b, AJ, 160, 124
Medina G. E. et al., 2018, ApJ, 855, 43
Miyamoto M., Nagai R., 1975, PASJ, 27, 533
Montuori M., Capuzzo-Dolcetta R., Di Matteo P., Lepinette A., Miocchi P., 2007, ApJ, 659, 1212
Muñoz R. R. et al., 2005, ApJ, 631, L137
Muñoz R. R. et al., 2006a, ApJ, 649, 201
Muñoz R. R. et al., 2006b, ApJ, 649, 201
Munoz R. R., Majewski S. R., Johnston K. V., 2008, ApJ, 679, 346
Muñoz R. R., Côté P., Santana F. A., Geha M., Simon J. D., Oyarzún G. A., Stetson P. B., Djorgovski S. G., 2018, ApJ, 860, 66
Muraveva T., Clementini G., Garofalo A., Cusano F., 2020, MNRAS, 499, 4040
Mutlu-Pakdil B. et al., 2018, ApJ, 863, 25
Mutlu-Pakdil B. et al., 2019, ApJ, 885, 53
Mutlu-Pakdil B. et al., 2020, ApJ, 902, 106
Navarro J. F., Frenk C. S., White S. D. M., 1996, ApJ, 462, 563
Newberg H. J. et al., 2002, ApJ, 569, 245
Pace A. B. et al., 2021, ApJ, 923, 77
Pace A. B., Li T. S., 2019, ApJ, 875, 77
Pace A. B. et al., 2020, MNRAS, 495, 3022
Palaversa L. et al., 2013, AJ, 146, 101
Penarrubia J., Navarro J. F., McConnachie A. W., Martin N. F., 2009, ApJ, 698, 222
Plummer H. C., 1911, MNRAS, 71, 460
Price-Whelan A. M., 2017, J. Open Source Softw., 2
Price-Whelan A. et al., 2020, adrn/gala: v1.3.
Reid M. J., Brunthaler A., 2004, ApJ, 616, 872
Riello M. et al., 2021, A&A, 649, A3
Rocha M., Peter A. H. G., Bullock J. S., 2012, MNRAS, 425, 231
Samus' N. N., Kazarovets E. V., Durlevich O. V., Kireeva N. N., Pastukhova E. N., 2017, Astron. Rep., 61, 80
Sesar B. et al., 2017, AJ, 153, 204
Shipp N. et al., 2018, ApJ, 862, 114
Simon J. D., 2018, ApJ, 863, 89
Simon J. D., 2019, ARA&A, 57, 375
Spencer M. E., Mateo M., Olszewski E. W., Walker M. G., McConnachie A. W., Kirby E. N., 2018, AJ, 156, 257
Strigari L. E., Frenk C. S., White S. D. M., 2018, ApJ, 860, 56
Stringer K. M. et al., 2021, ApJ, 911, 109
Torrealba G. et al., 2015, MNRAS, 446, 2251
Ural U., Wilkinson M. I., Read J. I., Walker M. G., 2015, Nat. Commun., 6, 7599
Vasiliev E., 2019, MNRAS, 489, 623
Virtanen P. et al., 2020, Nat. Methods, 17, 261
Vivas A. K., Mateo M., 2013, AJ, 146, 141
Vivas A. K. et al., 2004, AJ, 127, 1158
Vivas A. K., Alonso-García J., Mateo M., Walker A., Howard B., 2019, AJ, 157, 35
Walker M. G., Mateo M., Olszewski E. W., Gnedin O. Y., Wang X., Sen B., Woodroofe M., 2007, ApJ, 667, L53
Walker M. G., Mateo M., Olszewski E. W., 2009, AJ, 137, 3100
Walker M. G., Olszewski E. W., Mateo M., 2015, MNRAS, 448, 2717
Wang M. Y. et al., 2017, MNRAS, 468, 4887
Wang M. Y. et al., 2019, ApJ, 881, 118

APPENDIX A

This appendix provides information on the properties of the bright ($G < 19$) member candidates beyond the King limiting radius in each of the dSphs that we study in Tables A1 to A4.

Table A1. Possible member candidates beyond the King limiting radius for Draco and Ursa Minor. We only include stars with $P_{PM} \geq 0.9$, and the dust-corrected G magnitude: $G \leq 19$ mag. This table will be made available in its entirety in machine-readable form. The values for radial velocity V_r are taken from the work cited in Section 4.3.

Galaxy	Source ID	α [deg]	δ [deg]	$P_{\mathrm{Space}+PM}$	P_{PM}	V_r [km s^{-1}]	G [mag]	$\mu_\alpha cos\delta$ [mas yr^{-1}]	μ_δ [mas yr^{-1}]
Draco	1434492516786370176	261.909753	58.263091	0.864	0.978	−288.2	17.77	0.047 ± 0.127	−0.217 ± 0.138
	1433949770359264768	259.142130	58.498825	0.863	0.958	−292.3	18.68	0.093 ± 0.187	−0.206 ± 0.172
	1434014607185724544	260.617774	58.730676	0.600	0.936	–	18.75	−0.084 ± 0.186	−0.152 ± 0.197
	1433509931348820864	256.354218	57.552936	0.129	0.910	–	18.96	0.205 ± 0.184	−0.259 ± 0.281
	1422046732355091584	262.992811	56.621840	0.087	0.938	–	18.35	−0.093 ± 0.141	−0.311 ± 0.147
	1420524699025187328	261.600665	56.016370	0.048	0.937	–	17.89	−0.134 ± 0.116	−0.205 ± 0.110
	1435623055258755840	262.155953	59.890716	0.042	0.943	–	18.43	−0.057 ± 0.168	−0.066 ± 0.172
	1437346161777223936	258.784927	60.251350	0.022	0.931	–	18.99	−0.071 ± 0.202	−0.152 ± 0.227
	1432365034801179648	256.952365	55.751991	0.014	0.909	–	18.69	−0.149 ± 0.182	−0.159 ± 0.229
	1437470136009868416	260.717683	60.847082	0.009	0.928	–	18.96	−0.009 ± 0.221	−0.169 ± 0.251
Ursa Minor	1645171112311713536	228.351877	66.422532	0.990	0.999	–	16.14	−0.145 ± 0.041	0.066 ± 0.044
	1645606828153598848	230.260134	67.470024	0.988	0.997	–	16.77	−0.162 ± 0.059	0.069 ± 0.064
	1693470798398323328	225.704777	67.572588	0.988	0.995	–	17.12	−0.214 ± 0.068	0.099 ± 0.065
	1645270510739088000	227.326351	66.442343	0.985	0.994	−256.8	17.85	−0.097 ± 0.092	−0.012 ± 0.097
	1645194511293583616	229.300906	66.777715	0.983	0.997	–	16.42	−0.162 ± 0.046	0.042 ± 0.048
	1645185092429838592	228.491460	66.710679	0.976	0.991	–	17.19	−0.183 ± 0.077	0.177 ± 0.080
	1645204196444361728	228.979185	66.690191	0.974	0.995	–	17.25	−0.115 ± 0.080	0.002 ± 0.078
	1645635995276558336	230.874290	67.670574	0.972	0.995	–	17.12	−0.168 ± 0.059	0.136 ± 0.069
	1693464785444020224	224.677313	67.359829	0.936	0.988	–	17.78	−0.173 ± 0.094	−0.061 ± 0.105
	1693573430936780032	226.089830	67.779650	0.926	0.973	–	17.88	−0.220 ± 0.125	0.252 ± 0.107
	1693459013010166400	224.989988	67.202354	0.926	0.961	–	18.91	0.137 ± 0.216	0.050 ± 0.201
	1645948119139534336	230.439490	68.295812	0.919	0.985	–	18.24	−0.217 ± 0.156	0.058 ± 0.137
	1669324938936435200	224.507557	66.213615	0.919	0.978	–	18.21	−0.293 ± 0.142	0.168 ± 0.135
	1693484061257345792	224.702610	67.651446	0.866	0.986	–	17.95	−0.267 ± 0.102	0.136 ± 0.102
	1645527727740223744	230.409902	66.895595	0.850	0.987	–	18.58	−0.095 ± 0.156	0.151 ± 0.146
	1645257110440749696	227.204801	66.152029	0.836	0.973	–	18.94	−0.077 ± 0.193	−0.095 ± 0.209
	1645678017235803392	232.362738	67.876246	0.822	0.989	–	18.33	−0.075 ± 0.123	0.196 ± 0.133
	1693681908926278016	224.945984	67.943088	0.731	0.979	–	18.81	−0.193 ± 0.196	0.170 ± 0.193
	1693457849072756608	224.336427	67.494067	0.704	0.967	–	18.90	−0.266 ± 0.188	−0.080 ± 0.193
	1693636382271997056	223.382839	67.272458	0.698	0.977	–	18.69	−0.148 ± 0.166	0.254 ± 0.180
	1693671601004793984	224.122415	67.667227	0.692	0.977	–	18.61	−0.158 ± 0.187	0.219 ± 0.200
	1645155062017982848	228.595163	66.300722	0.636	0.962	–	18.94	−0.216 ± 0.208	−0.109 ± 0.232
	1669596518308786816	222.076584	66.913474	0.599	0.984	–	18.86	−0.134 ± 0.184	0.120 ± 0.171
	1645557655075852032	231.167407	67.175327	0.573	0.960	–	18.85	−0.074 ± 0.264	−0.106 ± 0.246
	1645221376313145728	226.395026	65.730813	0.571	0.956	–	18.61	−0.298 ± 0.234	0.289 ± 0.191
	1645064764625656064	227.457343	66.023662	0.562	0.948	–	18.81	−0.247 ± 0.200	−0.148 ± 0.178
	1645771063407500800	232.008520	68.238955	0.520	0.947	–	18.41	−0.210 ± 0.218	−0.107 ± 0.182
	1645042430795689344	226.810358	65.895622	0.440	0.911	–	18.40	0.031 ± 0.162	−0.231 ± 0.145
	1669619608053127168	223.195017	67.235376	0.336	0.930	–	18.66	−0.368 ± 0.160	−0.094 ± 0.192
	1621087886357153920	223.245645	64.770400	0.096	0.908	–	18.68	−0.428 ± 0.167	−0.094 ± 0.157

Table A2. Continued: possible bright ($G \leq 19$ mag) member candidates beyond the King limiting radius for Sextans and Sculptor.

Galaxy	Source ID	α [deg]	δ [deg]	$P_{Space+PM}$	P_{PM}	V_r [km s^{-1}]	G [mag]	$\mu_\alpha cos\delta$ [mas yr^{-1}]	μ_δ [mas yr^{-1}]
Sextans	3828856623037326464	153.378402	−2.388383	0.976	0.966	–	18.04	−0.308 ± 0.138	0.192 ± 0.143
	3829914043985259904	152.454533	−1.442343	0.975	0.970	–	18.04	−0.358 ± 0.171	−0.118 ± 0.147
	3830628451665548928	154.323570	−1.460667	0.972	0.979	–	17.77	−0.513 ± 0.162	0.177 ± 0.223
	3830708647294573824	154.132163	−0.962963	0.972	0.976	–	17.28	−0.561 ± 0.120	0.021 ± 0.133
	3828753990498353792	153.066253	−2.583271	0.969	0.976	–	18.58	−0.365 ± 0.192	−0.008 ± 0.182
	3830604331128780672	154.232532	−1.519406	0.954	0.958	–	17.58	−0.215 ± 0.149	−0.159 ± 0.209
	3831478820830542592	153.555006	−0.703581	0.953	0.949	–	18.85	−0.267 ± 0.260	0.191 ± 0.229
	3830319390113933952	154.654507	−2.160077	0.950	0.993	–	16.76	−0.411 ± 0.088	0.106 ± 0.085
	3830545339753349120	154.821339	−1.192598	0.948	0.990	–	17.50	−0.406 ± 0.109	0.109 ± 0.109
	3828858959499558144	153.494908	−2.299684	0.948	0.903	–	18.91	−0.609 ± 0.326	0.585 ± 0.462
	3830401608672381440	154.167771	−1.802013	0.947	0.953	–	18.91	−0.257 ± 0.271	0.009 ± 0.251
	3828950566856844288	153.172068	−2.426458	0.945	0.915	–	17.88	−0.314 ± 0.132	0.268 ± 0.124
	3830390720930784640	154.500820	−1.922632	0.943	0.985	–	16.88	−0.306 ± 0.104	−0.062 ± 0.152
	3829950705825803136	152.749148	−1.067950	0.922	0.915	231.53	18.67	−0.630 ± 0.213	−0.113 ± 0.207
	3828784987277714560	153.925853	−2.644071	0.913	0.980	–	17.01	−0.544 ± 0.090	0.154 ± 0.095
	3830602338263932928	154.212478	−1.583762	0.910	0.918	–	18.27	−0.602 ± 0.226	−0.077 ± 0.262
	3830816949190286080	154.618951	−0.547751	0.902	0.982	226.98	18.13	−0.440 ± 0.179	0.059 ± 0.147
	3831492186768793600	153.438987	−0.626571	0.880	0.923	231.39	18.54	−0.591 ± 0.226	−0.147 ± 0.211
	3830445181116015872	154.681072	−1.391989	0.877	0.963	–	17.64	−0.564 ± 0.146	0.263 ± 0.157
	3831551732195432576	153.463839	−0.440007	0.877	0.944	237.0	18.65	−0.522 ± 0.263	0.277 ± 0.249
	3828710083048013952	153.109300	−2.888955	0.873	0.959	–	18.65	−0.241 ± 0.240	0.135 ± 0.205
	3830740292613833856	154.685360	−1.027934	0.870	0.965	–	18.44	−0.403 ± 0.246	0.103 ± 0.229
	3831535553053384704	152.872744	−0.523191	0.861	0.959	–	18.19	−0.208 ± 0.199	−0.133 ± 0.204
	3831513459741694848	152.810584	−0.740800	0.829	0.910	–	18.68	−0.181 ± 0.355	−0.066 ± 0.434
	3830337287242365440	154.469507	−1.993393	0.754	0.927	–	18.50	−0.160 ± 0.261	−0.149 ± 0.347
	3831759406748927744	152.885667	−0.148648	0.753	0.967	–	18.24	−0.222 ± 0.184	−0.065 ± 0.175
	3831812247731524608	152.006430	0.018912	0.662	0.985	–	17.78	−0.410 ± 0.139	0.121 ± 0.123
	3780600603882398592	153.920001	−3.463134	0.543	0.968	–	18.04	−0.469 ± 0.231	0.207 ± 0.281
	3828582745857545856	151.638894	−2.787752	0.446	0.908	–	17.96	−0.212 ± 0.231	−0.311 ± 0.262
	3831259678714011008	155.039181	0.201047	0.278	0.922	–	18.10	−0.233 ± 0.174	−0.265 ± 0.172
	3833327202955907584	151.378337	0.067266	0.226	0.956	–	18.02	−0.173 ± 0.160	−0.019 ± 0.186
	3828376926729977984	151.580187	−3.824589	0.214	0.930	–	18.40	−0.398 ± 0.216	−0.196 ± 0.237
	3828173379639671680	151.843216	−3.932880	0.174	0.906	–	18.74	−0.198 ± 0.336	−0.140 ± 0.468
	3832339394837569152	154.075660	1.169582	0.127	0.913	–	18.70	−0.745 ± 0.239	0.149 ± 0.246
Sculptor	5026328277217292416	16.299378	−34.384139	0.992	0.999	95.78	18.27	0.186 ± 0.119	−0.098 ± 0.103
	5027479362811922048	14.921115	−32.834462	0.987	0.997	–	18.27	−0.142 ± 0.135	−0.087 ± 0.090
	5026130884816022016	16.843514	−34.664602	0.985	1.000	118.78	17.82	0.039 ± 0.089	−0.088 ± 0.076
	5002282889926690944	15.894926	−34.914193	0.980	0.999	–	17.40	0.177 ± 0.082	−0.241 ± 0.066
	5006419626331394048	12.675394	−33.468379	0.980	0.999	–	17.59	0.077 ± 0.103	−0.176 ± 0.121
	5026553230423938816	16.880088	−33.216605	0.964	0.998	–	18.78	−0.093 ± 0.147	−0.147 ± 0.139
	5003074675736263936	13.984518	−34.337675	0.930	0.991	–	18.78	0.313 ± 0.200	−0.459 ± 0.185
	5006627262230333568	11.912982	−32.941090	0.660	0.995	–	18.94	0.008 ± 0.190	0.138 ± 0.235
	5002261342074627968	15.575382	−35.183082	0.514	0.980	–	18.78	0.365 ± 0.105	−0.018 ± 0.136
	4989939561938365056	16.437265	−36.393187	0.021	0.920	–	18.92	0.457 ± 0.127	0.030 ± 0.156

Table A3. Continued: possible bright ($G \leq 19$ mag) member candidates beyond the King limiting radius for Fornax.

Galaxy	Source ID	α [deg]	δ [deg]	$P_{Space+PM}$	P_{PM}	V_r [km s^{-1}]	G [mag]	$\mu_\alpha cos\delta$ [mas yr^{-1}]	μ_δ [mas yr^{-1}]
Fornax	5050579243118343424	41.157190	−34.431349	0.999	1.000	–	18.24	0.289 ± 0.081	−0.291 ± 0.117
	5062736616203680384	40.533001	−33.205159	0.999	1.000	–	18.23	0.391 ± 0.070	−0.313 ± 0.118
	5062705000946431872	40.217350	−33.409180	0.999	1.000	–	18.42	0.332 ± 0.079	−0.205 ± 0.137
	5062893812007463680	40.124558	−33.341377	0.999	1.000	–	18.17	0.367 ± 0.067	−0.480 ± 0.114
	5050045017906217600	39.601695	−35.497694	0.999	1.000	59.16	18.76	0.460 ± 0.123	−0.422 ± 0.181
	5062050173052716288	39.425662	−35.460194	0.999	1.000	70.80	18.64	0.395 ± 0.106	−0.193 ± 0.160
	5050631126322947456	41.375949	−33.930902	0.998	1.000	–	18.69	0.455 ± 0.094	−0.259 ± 0.139
	5062595225880065280	39.304869	−33.132383	0.998	1.000	–	17.87	0.352 ± 0.052	−0.300 ± 0.095
	5050059998752238848	40.353540	−35.314325	0.997	0.999	53.54	18.66	0.289 ± 0.102	−0.108 ± 0.148
	5062921261140200704	39.988323	−33.043346	0.997	1.000	–	18.20	0.278 ± 0.064	−0.278 ± 0.110
	5062116418628357888	39.009953	−35.297152	0.997	0.999	–	18.84	0.374 ± 0.106	−0.590 ± 0.162
	5062400711103888000	38.477085	−34.427507	0.997	1.000	–	17.76	0.288 ± 0.054	−0.245 ± 0.086
	5050747262238524288	41.914633	−33.274775	0.996	1.000	–	18.11	0.409 ± 0.071	−0.427 ± 0.116
	5050146447853774592	41.076959	−34.831323	0.996	0.999	–	18.63	0.326 ± 0.100	−0.109 ± 0.143
	5062382053765788800	38.886398	−34.276573	0.996	0.999	–	19.00	0.276 ± 0.116	−0.026 ± 0.204
	5050008974540402304	40.355478	−35.530882	0.995	0.999	–	18.85	0.300 ± 0.129	−0.465 ± 0.168
	5050022649716434560	39.921591	−35.768959	0.995	0.999	–	18.86	0.236 ± 0.135	−0.288 ± 0.175
	5062334499888230400	38.686711	−34.704170	0.995	0.999	64.02	17.98	0.514 ± 0.066	−0.489 ± 0.101
	4965973781866201088	39.223780	−35.576720	0.994	0.999	–	18.98	0.189 ± 0.139	−0.428 ± 0.193
	5050584981194691072	41.292742	−34.361836	0.993	0.998	–	18.57	0.184 ± 0.091	−0.193 ± 0.137
	5063031281023014016	40.797560	−32.763278	0.992	1.000	–	18.50	0.396 ± 0.074	−0.533 ± 0.132
	5050148200201001216	41.183856	−34.796284	0.989	0.998	–	18.42	0.190 ± 0.092	−0.307 ± 0.138
	5062327868458705152	38.673459	−34.901775	0.989	0.997	42.14	18.96	0.208 ± 0.125	0.062 ± 0.195
	5050053298603169152	40.058157	−35.496765	0.983	0.996	–	18.65	0.558 ± 0.112	−0.663 ± 0.150
	5049893113502647552	41.017739	−35.709940	0.981	0.999	–	18.91	0.257 ± 0.137	−0.383 ± 0.182
	5049899126456915584	41.167672	−35.628223	0.976	0.999	–	18.83	0.436 ± 0.130	−0.531 ± 0.181
	4966282744633038976	37.596957	−34.988158	0.976	0.999	–	18.23	0.249 ± 0.070	−0.218 ± 0.108
	4953602734161644672	40.462090	−36.953337	0.927	0.999	–	18.94	0.395 ± 0.141	−0.439 ± 0.197
	5063569255744340992	37.411716	−32.515749	0.866	1.000	–	18.28	0.278 ± 0.083	−0.254 ± 0.128
	5049970972669630464	40.059478	−35.905110	0.794	0.982	–	18.42	0.587 ± 0.097	−0.153 ± 0.137

Table A4. Continued: possible bright ($G \leq 19$ mag) member candidates beyond the King limiting radius for Carina.

Galaxy	Source ID	α [deg]	δ [deg]	$P_{Space+PM}$	P_{PM}	V_r [km s^{-1}]	G [mag]	$\mu_\alpha cos\delta$ [mas yr^{-1}]	μ_δ [mas yr^{-1}]
Carina	5502112320339516672	101.801148	−50.858992	0.902	0.962	237.7	17.23	0.430 ± 0.078	0.208 ± 0.085
	5502484603810420096	98.874167	−51.559791	0.848	0.966	–	17.60	0.460 ± 0.096	0.205 ± 0.095
	5502134271915130752	102.268094	−51.070889	0.823	0.982	–	17.43	0.510 ± 0.084	0.195 ± 0.085
	5502698046503172608	99.017039	−51.051548	0.778	0.901	–	18.74	0.687 ± 0.173	0.258 ± 0.160
	5501694707782516992	99.904891	−51.692459	0.757	0.909	–	18.71	0.673 ± 0.166	0.226 ± 0.188
	5502715157652966912	98.843143	−50.915351	0.699	0.925	–	18.37	0.492 ± 0.139	0.275 ± 0.144
	5503082845509707264	102.633411	−49.614035	0.661	0.991	–	16.81	0.558 ± 0.057	0.095 ± 0.059
	5502003292595409792	101.300724	−51.628797	0.619	0.942	–	18.35	0.419 ± 0.143	0.071 ± 0.143
	5502783086856009472	98.546699	−50.644352	0.361	0.910	–	18.45	0.390 ± 0.143	0.106 ± 0.190
	5503162968122548864	101.382482	−49.778490	0.334	0.916	–	18.65	0.619 ± 0.150	0.276 ± 0.178
	5502321601210343552	98.433843	−52.066497	0.284	0.914	–	18.77	0.667 ± 0.160	−0.039 ± 0.179
	5502693201779934336	98.332298	−50.618324	0.255	0.903	–	18.63	0.423 ± 0.179	0.202 ± 0.215
	5550731689430964864	98.113615	−50.601210	0.251	0.928	–	18.31	0.678 ± 0.147	0.005 ± 0.154
	5507927225023057920	104.068619	−50.782767	0.146	0.957	–	17.75	0.538 ± 0.129	0.049 ± 0.115
	5551333431529187712	100.284868	−48.954146	0.135	0.974	–	18.12	0.553 ± 0.116	0.089 ± 0.114
	5551161568414174592	99.067310	−49.096048	0.128	0.980	–	17.24	0.622 ± 0.068	0.062 ± 0.074
	5503091538523737856	102.962540	−49.427400	0.118	0.925	–	18.27	0.402 ± 0.141	0.019 ± 0.149
	5498748841255266304	102.372292	−52.200728	0.094	0.940	–	18.01	0.408 ± 0.124	0.043 ± 0.135
	5503316968470246016	102.418646	−48.895997	0.092	0.953	–	18.15	0.582 ± 0.127	0.199 ± 0.161
	5501115746195240960	96.526764	−51.811424	0.087	0.927	–	18.48	0.555 ± 0.150	0.266 ± 0.162
	5500861621573059200	96.769550	−52.268656	0.085	0.927	–	18.49	0.515 ± 0.173	−0.029 ± 0.156
	5508291227794323456	104.291538	−49.549433	0.082	0.946	–	18.13	0.619 ± 0.126	0.168 ± 0.157
	5508226567063203456	104.582542	−49.788463	0.079	0.949	–	17.11	0.411 ± 0.070	0.224 ± 0.107
	5508223199808847616	104.542154	−49.855331	0.070	0.938	–	18.15	0.492 ± 0.132	0.281 ± 0.194
	5501047301592401792	96.267243	−52.214214	0.065	0.932	–	18.55	0.509 ± 0.216	0.062 ± 0.166
	5498030654002855168	100.777890	−53.922374	0.060	0.987	–	16.61	0.486 ± 0.064	0.111 ± 0.056
	5498842162304146432	103.086474	−51.882643	0.056	0.907	–	18.78	0.517 ± 0.237	0.155 ± 0.227
	5509107065421158912	103.469718	−48.969735	0.053	0.929	–	18.70	0.490 ± 0.166	0.262 ± 0.173
	5501709894786503040	100.809104	−52.794495	0.053	0.913	–	18.58	0.501 ± 0.165	0.310 ± 0.191
	5551317114950058496	101.100594	−48.724560	0.050	0.940	–	17.97	0.484 ± 0.115	−0.045 ± 0.143
	5498321784065583232	100.374342	−53.109248	0.042	0.929	–	18.43	0.548 ± 0.205	0.121 ± 0.194
	5498583781367476480	103.555969	−52.610894	0.038	0.963	–	17.57	0.401 ± 0.092	0.174 ± 0.098
	5504916757888065152	104.810045	−51.081224	0.037	0.929	–	18.49	0.555 ± 0.189	0.226 ± 0.196
	5503327997946913792	102.974485	−48.588524	0.035	0.929	–	18.47	0.621 ± 0.196	0.177 ± 0.164
	5501271945562728576	98.379568	−53.238275	0.030	0.903	–	17.97	0.594 ± 0.130	−0.077 ± 0.143
	5504817084584768256	104.635657	−51.654347	0.026	0.927	–	17.94	0.387 ± 0.110	0.033 ± 0.113
	5498252377393951488	100.410125	−53.444287	0.017	0.902	–	18.78	0.457 ± 0.187	0.296 ± 0.202
	5551187024683306624	98.461590	−49.023626	0.017	0.901	–	18.58	0.726 ± 0.152	0.203 ± 0.151
	5498511144880789632	103.921354	−53.008845	0.010	0.928	–	18.04	0.678 ± 0.119	0.158 ± 0.130

This paper has been typeset from a TEX/LATEX file prepared by the author.